

# New Technologies for Optical Coherence Microscopy

by

**Shu-Wei Huang**

B.E., Electrical Engineering  
National Taiwan University, 2005

Submitted to the

DEPARTMENT OF ELECTRICAL ENGINEERING AND COMPUTER SCIENCE

in partial fulfillment of the requirements for the degree of

MASTER OF SCIENCE

at the

MASSACHUSETTS INSTITUTE OF TECHNOLOGY

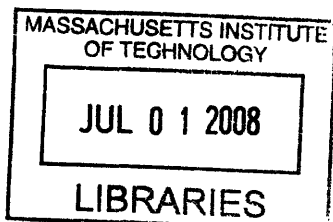
June 2008

© Massachusetts Institute of Technology 2008  
All rights reserved

Signature of Author \_\_\_\_\_  
Department of Electrical Engineering and Computer Science  
May 2008

Certified by \_\_\_\_\_  
Professor James G. Fujimoto  
Thesis Supervisor

Accepted by \_\_\_\_\_  
Professor Terry P. Orlando  
Chairman, Department Committee on Graduate Students



**ARCHIVES**



# **New Technologies for Optical Coherence Microscopy**

by

**Shu-Wei Huang**

Submitted to the Department of Electrical Engineering and Computer Science  
on May 1, 2008 in partial fulfillment of the  
requirements for the Degree of Master of Science in  
Electrical Engineering and Computer Science

## **ABSTRACT**

According to the American Cancer Society, gastrointestinal (GI) cancers are among the most common forms of malignancies suffered today, affecting ~200,000 people and causing ~80,000 deaths in the United States every year. The prognosis depends heavily on the detection of early-stage lesions. The process of endoscopic surveillance, excisional biopsy, and histologic examination is the current gold standard for screening and diagnosis of many GI cancers. This process, however, is invasive, time-consuming, and can suffer from unacceptable false negative rates. Optical imaging technology that provides real-time, high-resolution imaging of human tissue *in vivo* with resolution at or near that of histopathology may significantly improve clinicians' capabilities to identify malignancies at curable stages. The ability to assess histologic hallmarks of GI cancer at the tissue architectural and cellular levels without excisional biopsy would be a major advance in GI cancer management.

Development of techniques to reliably image cellular and subcellular structure through endoscopic devices is one of the most outstanding challenges in biomedical imaging today and holds tremendous promise for surgical applications and for early diagnostic screening and staging of epithelial malignancies. Optical coherence microscopy (OCM) is an *in vivo* cellular imaging technique that combines OCT with confocal microscopy. Due to the unique feature of using two distinct optical sectioning techniques, OCM can provide superior imaging depth in highly scattered tissues and can overcome important imaging probe design limitations that hinder confocal microscopy. Two novel designs for OCM systems are proposed and developed for high resolution cellular imaging. The first uses Fourier domain optical coherence detection, and the second implements line-field illumination and detection. Differences in performance from the standard time-domain optical coherence microscopy systems will be studied.

Thesis Supervisor: James G. Fujimoto  
Professor of Electrical Engineering and Computer Science

## **ACKNOWLEDGEMENTS**

I would like to thank my thesis advisor, Professor James Fujimoto, for providing the guidance and the resources necessary to complete this work. His keen scientific insight, tireless attention to detail, and careful mentoring inspire me personally and professionally and I am grateful for the opportunity to work with him.

I would also like to thank all my colleagues in the Ultrafast Optics Group at MIT. Together they create an exciting and supportive environment for scientific research. I want to acknowledge especially the help from Aaron Aguirre, Yu Chen, Desmond Adler, and Robert Huber. My thesis work could not have been completed without the technical support and friendship of them. I gratefully thank all my friends from MIT for providing the necessary diversions to keep me sane during the past two years. I endlessly thank my parents, my siblings, and my girlfriend for the unconditional support.

## TABLE OF CONTENTS

|   |           |
|---|-----------|
| <b>Abstract.....</b>  | <b>3</b>  |
| <b>Acknowledgements .....</b>   | <b>4</b>  |
| <b>Table of Contents .....</b>  | <b>5</b>  |
| <br>  |           |
| <b>Chapter 1: Introduction</b>  | <b>7</b>  |
| 1.1 <b>Optical Coherence Tomography .....</b>                                 | <b>7</b>  |
| 1.2 <b>Endoscopic Optical Coherence Tomography .....</b>                      | <b>7</b>  |
| 1.3 <b>Ultrahigh Resolution Endoscopic Optical Coherence Tomography .....</b> | <b>8</b>  |
| 1.4 <b>Confocal Fluorescence Endomicroscopy .....</b>                         | <b>10</b> |
| 1.5 <b>Optical Coherence Microscopy .....</b>                                 | <b>11</b> |
| 1.6 <b>Scope of the thesis .....</b>  | <b>13</b> |
| <b>Figures .....</b>  | <b>15</b> |
| <b>References .....</b>   | <b>21</b> |
| <br>  |           |
| <b>Chapter 2: Swept Source Optical Coherence Microscopy</b>                   | <b>25</b> |
| 2.1 <b>Confocal Based Optical Coherence Microscopy .....</b>                  | <b>25</b> |
| 2.2 <b>High Speed Swept Source Optical Coherence Tomography .....</b>         | <b>26</b> |
| 2.3 <b>Fourier-domain Mode-locked Laser .....</b>                             | <b>27</b> |
| 2.4 <b>Swept Source Optical Coherence Microscopy .....</b>                    | <b>28</b> |
| 2.5 <b>Analog Demodulation Scheme for Real-time Display .....</b>             | <b>34</b> |
| <b>Figures .....</b>  | <b>38</b> |
| <b>References .....</b>   | <b>48</b> |

|   |           |
|---|-----------|
| <b>Chapter 3: Line Scan Optical Coherence Microscopy</b>                  | <b>53</b> |
| <b>3.1 Linnik type Optical Coherence Microscopy .....</b>                 | <b>53</b> |
| <b>3.2 Line Scan Optical Coherence Microscopy .....</b>                   | <b>53</b> |
| <b>3.3 Future Work .....</b>  | <b>58</b> |
| <b>3.4 Preliminary Comparison between Three OCM Imaging Systems .....</b> | <b>60</b> |
| <b>Figures .....</b>  | <b>63</b> |
| <b>References .....</b>   | <b>73</b> |
| <br>  |           |
| <b>Chapter 4: Summary</b>   | <b>75</b> |

# CHAPTER 1 – INTRODUCTION

## 1.1 Optical Coherence Tomography

Optical coherence tomography (OCT) is an emerging medical imaging technology which enables micron scale, cross-sectional and three-dimensional imaging of tissue architecture in situ and in real time [1-3]. OCT forms cross-sectional images in scattering tissue by using a Michelson interferometer and a broad bandwidth light source to select reflected light from a small volume, a method known as coherence gating. Figure 1 illustrates the principle of coherence gating used in OCT. Light from a broad bandwidth source is divided into a scanning reference path and a sample path. The backscattered light probing the sample is recombined with the reference path light at a photodetector to produce interference fringes. Interference will only be seen when the reference path length matches the sample path length to within the coherence length of the light source, which is inversely proportional to the optical bandwidth. In other words, the interference fringes will only carry sample information at a certain depth and hence provide optical sectioning capability. Standard OCT has an axial resolution of  $\sim 10 \mu\text{m}$ , but ultrahigh axial resolution of  $1\text{-}2 \mu\text{m}$  can be achieved using state-of-the-art broad bandwidth laser technologies [4-7]. The optical sectioning capability of OCT is comparable to the standard  $5 \mu\text{m}$  histologic section thickness. In addition, OCT performs optical heterodyne detection similar to that used in optical communications, which enables extremely high sensitivities near the quantum limit. Imaging depth of  $1\text{-}2 \text{ mm}$ , which is sufficient for evaluation of early neoplastic changes in carcinomas, has been demonstrated in human GI tissues [2].

Example OCT images are shown in Figure 2. Two-dimensional cross-sectional images of tissue are constructed by laterally scanning the optical beam and performing sequential axial measurements of backscattered light at different transverse positions. The beam is scanned under computer control and the resulting data set is a two-dimensional array which represents the optical backscattering or reflection within a cross-sectional slice of the tissue specimen. This data can be digitally filtered, processed, and displayed as a two-dimensional gray scale or false color image. Three-dimensional images can also be constructed by acquiring a series of two-dimensional images in a similar way as CT.

## 1.2 Endoscopic Optical Coherence Tomography

OCT imaging can be performed endoscopically using fiber-optic imaging catheters introduced into the biopsy port of standard endoscopes. Endoscopic OCT (EOCT) imaging was first demonstrated in 1997 by Tearney *et al.* in a rabbit's gastrointestinal and pulmonary tract. The concept of optical biopsy and its clinical applications including screening of Barrett's esophagus (BE) and ulcerative colitis (UC) were proposed [8]. At the end of the year, EOCT imaging in human patients was demonstrated by Sergeev *et al.*, showing that all layers of the esophageal wall can be identified and disruption of the well-defined stratified mucosa is observed in cancerous lesions [9]. Jackle *et al.* later described a feasibility study of EOCT imaging in esophageal disorders, including reflux esophagitis, BE, and adenocarcinoma. Distinct patterns of normal, inflammatory, premalignant, and malignant tissues can be identified in OCT images [10]. A statistical study to establish the sensitivity and specificity of OCT for diagnosing specialized intestinal metaplasia (SIM) in BE was reported in 2001. Poneros *et al.* developed OCT image criteria for SIM in BE and 97% sensitivity and 92% specificity was achieved [11]. Evans *et al.* further developed a scoring system to differentiate intramucosal carcinoma and high-grade dysplasia (IMC/HGD) from low-grade dysplasia (LGD) and SIM, reporting 83% sensitivity and 75% specificity for diagnosing IMC/HGD [12].

EOCT imaging in human colon was demonstrated by Rollins *et al.* in 1999 [13]. Feasibility studies of EOCT imaging in colonic disorders, including hyperplastic polyp, adenoma, and carcinoma, were later demonstrated by Jackle *et al.* and Pfau *et al.* [14, 15]. Features based on polyp organization, mucosal architecture, and light scattering were identified in OCT images to distinguish between different lesions. Using the presence of disrupted layered structures on OCT images as the criterion, Shen *et al.* reported an accuracy of 87% to distinguish Crohn's disease from UC [16]. Familiari *et al.* later identified three OCT patterns for UC and the diagnostic sensitivity and specificity achieved 100% and 69%, respectively [17]. These studies demonstrate that OCT imaging can be readily integrated with endoscopic procedures and provides useful clinical information.

### **1.3 Ultrahigh Resolution Endoscopic Optical Coherence Tomography**

Figure 3 is a schematic of the ultrahigh resolution EOCT system that our group developed in collaboration with LightLab Imaging [18]. A custom-built femtosecond Cr<sup>4+</sup>:Forsterite laser with 180 nm bandwidth centered at ~1260 nm was used to provide ~4  $\mu$ m axial resolution, a

three- to four-fold improvement over standard EOCT systems. Enhanced image resolution and reduced speckle size enable ultrahigh resolution EOCT to visualize the increase of tissue architectural heterogeneity correlated with the progression of pathology more clearly than standard resolution EOCT (see Figure 4). A high speed depth scanner was used in the reference arm to provide real-time imaging at 4 cross-sectional images per second. Polarization controllers were used in both the sample and reference arms to optimize the interference strength. To match the optical dispersion between the two arms of the interferometer to achieve ultrahigh axial resolution, dispersion compensating glass (DCG) was inserted in the reference arm, and an air-gap coupling (AGC) was used in the sample arm. The back-reflected EOCT signal was split into two orthogonal polarization dependent channels by a polarizing beam splitter (PBS), and the two detector outputs were digitally demodulated. A polarization diversity signal was obtained by vector summation of two orthogonal channels' signals. Figure 5 shows photos of the EOCT system as well as the imaging catheter.

Working in collaboration with Dr. Hiroshi Mashimo, MD, PhD, at the VA Boston Healthcare System, our group performed clinical ultrahigh resolution EOCT studies [19]. Imaging was performed by introducing the EOCT imaging probe into the endoscope working channel, providing simultaneous endoscopic and EOCT views (see Figure 5). Figure 6 shows representative ultrahigh resolution EOCT images of the human esophagus. Figure 6A shows normal squamous epithelium with a characteristic layered architecture. Figure 6C shows a representative image of Barrett's esophagus. EOCT images of Barrett's esophagus show clear differences in architectural morphology compared to normal esophageal squamous mucosa. The layered architecture is replaced by glandular structures and low-backscattering Barrett's glands are observed in the mucosa with interlaced regions of high-backscattering connective tissue corresponding to the lamina propria. Figure 6E shows a representative EOCT image of high-grade dysplasia. High-grade dysplasia is characterized by irregular, distorted, and cribriform or villiform glandular architecture and is more heterogeneous than non-dysplastic Barrett's epithelium. Figure 6G shows an EOCT image of esophageal adenocarcinoma with epithelial disruption and stromal infiltration extending from the superficially ulcerated carcinoma. EOCT images show progressive increase in architectural irregularity from Barrett's mucosa to high-grade dysplasia and eventually to adenocarcinoma. Overall, ultrahigh resolution EOCT images showed good correlation with architectural morphology in histology (see Figure 6 B, D, F, H).

EOCT can also visualize the submucosa, which cannot be seen with endoscopy. Figure 7A shows esophageal adenocarcinoma underneath benign squamous epithelium in a patient 15 months after photodynamic therapy. The irregularly backscattering adenocarcinoma is dramatically different from normal squamous mucosa and Barrett's metaplasia. EOCT images of adenocarcinoma show irregularly shaped and crowded glandular architecture underneath the smooth squamous epithelium, as confirmed by histology (Figure 7B). Figure 7C shows an EOCT image in a patient 6 months after bi-polar radiofrequency ablation therapy. EOCT reveals squamous neo-epithelium similar to that observed from normal esophagus. However, glandular structures characteristic of Barrett's esophagus can be seen under the smooth-appearing epithelium. The presence of subsquamous Barrett's was confirmed by corresponding biopsy and histology (Figure 7D). EOCT allows real-time *in vivo* imaging of subsurface tissue morphology which promises to enable assessment of treatment efficacy after ablation therapy. This suggests that EOCT could be a promising non-invasive tool in evaluation of therapy and for real time guidance of focal ablation during follow-up endoscopy.

Despite promising results with endoscopic OCT, the technique has been limited by the lack of sufficient transverse resolution to resolve cellular features. The transverse resolution of OCT is typically 15-25  $\mu\text{m}$ , which is about the same as the size of human epithelial cells, and thus some clinically important features such as cell shape and nucleus-to-cytoplasm ratio cannot be identified in OCT images. A cellular resolution imaging technique that can be integrated with both endoscopic procedures and OCT would be an important step toward the ultimate goals of *in vivo* optical biopsy and guidance of excisional biopsy.

#### **1.4 Confocal Fluorescence Endomicroscopy**

With the advances in confocal fluorescence endomicroscopy, the concept of *in vivo* optical imaging diagnosis of dysplasia and cancer, as well as targeted biopsy, is becoming feasible and promises to significantly impact clinical care management strategies [20, 21]. Due to the low backscattering of human tissues, optical techniques in general suffer from low signal to noise ratio and thus high speed *in vivo* imaging is prohibited. Confocal fluorescence microscopy solves the problem by adding contrast agents to boost the signal level, a technique used routinely by pathologists, and excellent *in vivo* images showing cellular structure have been demonstrated. Nevertheless, it has a number of inherent disadvantages. First, the method relies on the use of

intravenous or topically applied stains, each of which has potential toxicity. Although fluorescein is one of the few FDA approved contrast agents, studies show that a few percent of the treated patients will suffer from nausea, vomit, and rash even with a mild dose (10% 5mL) [22]. Justification of its use in angiography is being reexamined recently [23, 24]. Consequently, there exists a compromise between the dosage of contrast agents, which relates to safety consideration, and the imaging speed. Efficient and biocompatible contrast agents will resolve the compromise, but the development is technically challenging and may not be available in the near future. Second, achieving sufficient confocal sectioning requires high quality, high numerical aperture (NA) objective lenses, which makes probe devices expensive and miniaturization difficult. Use of high NA optics also limits the field of view. As a result, some investigators have proposed using OCT together with confocal microscopy to provide a larger field of view [25]. Combining OCT with confocal fluorescence microscopy is challenging, however, because the two systems require entirely different light sources, optics, and detection electronics. Last but not the least; the penetration depth is limited fundamentally. Current penetration depth of confocal fluorescence microscopy is limited to 100-150  $\mu\text{m}$  in GI tract [26, 27] and therefore can not accurately assess the basement membrane integrity for invasion of malignant cells into the underlying supportive tissues. The ability to maintain sufficient optical sectioning power to isolate a single layer of cells for visualization determines the penetration depth. The sectioning power of confocal fluorescence microscopy depends solely on tight focusing and therefore it is vulnerable to severe aberration and multiple scattering in human tissues. Waveform modulation by adaptive optics technology is a promising method to extend the penetration depth of confocal fluorescence microscopy. However, it not only increases the system complexity but also decreases the imaging speed significantly.

### **1.5 Optical Coherence Microscopy**

Optical coherence microscopy (OCM) is a derivative of OCT which can extend the transverse resolution to achieve cellular level resolution [28, 29]. Figure 8 depicts the key difference between OCT and OCM, which leads to distinct system designs. OCM uses optics with a higher numerical aperture, usually around 0.3-0.4, to focus the light to small spot size onto the sample and achieve a transverse resolution of  $\sim 1\text{-}2\ \mu\text{m}$ . The defocusing effect, however, is much more severe, and the effective imaging range (green box) is limited to  $\sim 20\ \mu\text{m}$  around the

focus while that of OCT is on the order of millimeters. To overcome the depth of field restriction imposed by high NA focusing, OCM uses 2D raster scanning to generate an *en face* view. Instead of a depth scanner, a phase modulator is used in the reference arm to generate interference signals. Figure 9 shows a schematic of the high speed OCM system published by Aguirre *et al.* in 2003 [29]. *In vivo* imaging at 4 *en face* views per second with  $\sim 2$   $\mu\text{m}$  transverse resolution and  $\sim 3$   $\mu\text{m}$  axial resolution was demonstrated. The results are significant because they show that *in vivo* cellular level imaging is possible using a modified implementation of OCT. The use of coherence gating to perform depth sectioning enables use of lower NA microscope optics compared to other *in vivo* microscopy techniques such as confocal microscopy, which makes OCM more suitable for endoscopic imaging.

During the past few years, our group made significant advances to enable clinical applications of OCM. Previous OCM systems were difficult to use outside the laboratory due to system complexity. Using theoretical modeling and experimental studies, we developed compact laser sources for ultrahigh resolution OCT and OCM using commercially available femtosecond lasers and continuum generation in highly nonlinear optical fibers [30, 31]. These light sources provide axial coherence resolutions of  $<5$   $\mu\text{m}$  and are suitable for use in the clinic. For OCM imaging, a compact femtosecond laser at 1060 nm wavelength was incorporated into a novel fiber-based system using a broadband electro-optic phase modulator and novel dispersion control techniques (see Figure 10). A computer interface controls the system, including a fiber-optic scanning confocal microscope. The design also incorporates an active reference arm path length control, which is used for rapid, automated coordination of the optical coherence gate with the focal plane. This feature compensates for optical path length fluctuations from tissue heterogeneity. The control algorithm is analogous to auto-focusing strategies used in modern digital cameras, and ensures optimal image quality during real-time imaging.

Figure 11 highlights the ability for OCM to visualize cellular structure important for cancer detection. Images were acquired with  $<4$   $\mu\text{m}$  axial and  $<2$   $\mu\text{m}$  transverse image resolutions over a field of view of  $400$   $\mu\text{m}$  x  $400$   $\mu\text{m}$  at a frame rate of 2 frames/second. OCM images of squamous epithelium from the normal human esophagus *ex vivo* show cellular level resolution with expected variations in cell size, organization, and nuclear-to-cytoplasm ratio with depth. Figure 12 shows OCM images of lower GI pathologies for comparison with the normal colon (A,D). The dysplastic adenomatous polyp in (B,E) exhibits elongated, elliptical-shaped crypts

with thickened epithelium, while the colonic adenocarcinoma in (C,F) shows highly irregular glandular morphology and highly scattering foci of nuclei in a heterogeneous stroma. Results from these studies demonstrate that cellular resolution provided by OCM generates complementary information to ultrahigh resolution OCT and has the potential to dramatically improve the ability for early cancer detection.

OCM can be readily combined with OCT to enable imaging of architectural as well as cellular features. A combined OCT and OCM system requires that the magnification of the optical imaging probe be variable, similar to the way in which a conventional bench microscope has an objective turret for variable magnification. With ongoing advances in miniaturized optics and variable focus lens technology, it is feasible that OCT and OCM will be available in one endoscopic units in the near future.

## **1.6 Scope of the thesis**

The theme of this thesis is the development of OCM technologies for *in vivo* cellular resolution imaging. Two novel designs for OCM systems are proposed and developed. The first uses Fourier domain optical coherence detection, and the second implements line-field illumination and detection. Differences in performance from the standard time-domain optical coherence microscopy systems will also be studied.

Chapter 2 starts with a brief introduction of Fourier-domain OCT and Fourier domain mode locked (FDML) laser. Fourier-domain OCT using FDML laser as the source has achieved record high speed OCT imaging at 370,000 axial scan per second [32]. The advances in imaging speed not only greatly improve the tissue coverage, but are key to enabling *in vivo* 3D-OCT. 3D-OCT promises to be a powerful technology because it enables new visualization and processing techniques. The chapter goes on to describe a newly developed OCM system which is termed swept source OCM (SS-OCM) and presents a summary of imaging results. Different from most of the OCM investigations performed to date, SS-OCM uses the Fourier-domain detection method and FDML laser. The results are significant because they show that cellular level imaging is possible using Fourier-domain OCT methods. This simplifies the optical design for the OCM system at the expense of increased complexity in the detection electronics and the need for increased computing power. Because of the high computing load required for swept-source

OCM, real-time display is difficult to achieve. To address this issue, an analog demodulation scheme that might enable real-time display is proposed.

Chapter 3 discusses development of another new technology for OCM, termed line-scan OCM (LS-OCM). The chapter will start with a description on the image formation theory of LS-OCM. LS-OCM is a variation of full-field OCM, which has been widely investigated in recent years due to its simplicity and low-cost [33-36]. Compared with full-field OCM, LS-OCM implements line illumination and detection to reduce incoherent scattered light and pixel cross-talk and therefore has higher sensitivity to achieve cellular imaging in highly scattered tissues. The chapter goes on to describe the imaging system and presents a summary of imaging results. The results are significant because they show that cellular level imaging is possible using the OCM system with a single-axis scanning. The development of high performance, miniaturized single-axis scanning devices may prove less challenging technologically than the two-axis scanners required by time domain OCM and SS-OCM, and therefore LS-OCM may facilitate the development of endoscopic OCM. It follows to discuss the modulation / demodulation scheme and the selection of camera as well as the optical design, which determines the performance of LS-OCM. The chapter ends with a preliminary comparison of standard time domain OCM, SS-OCM, and LS-OCM. Finally, chapter 4 summarizes the results and discusses future work.

**Figures**

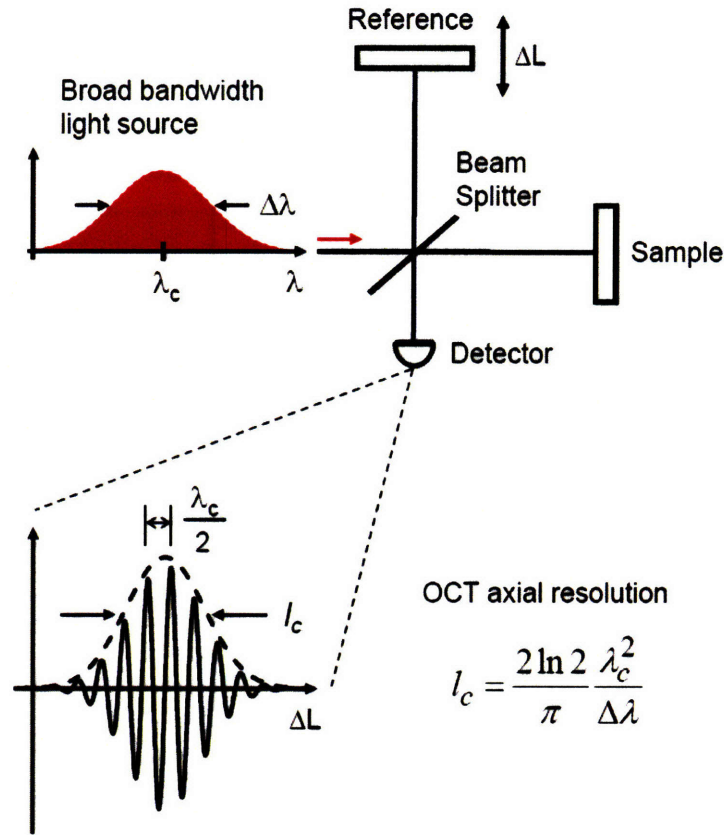


**Figure 1.** Schematic illustrating the principle of coherence gating. A Michelson interferometer is used to combine light from the sample with light passing through a scanning reference path. For broadband light sources, interference is seen only when the reference path length matches the sample path length to within the coherence length of the light source.

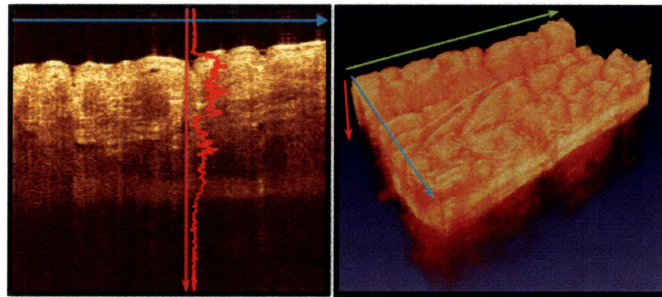


**Figure 2.** Description of the formation of an OCT image. The backscattered intensity (red curve) is mapped as a function of depth. A 2D cross-sectional image is formed by laterally scanning the optical beam on the sample. A 3D volumetric image can also be generated by stacking a series of 2D images in a similar way as CT.

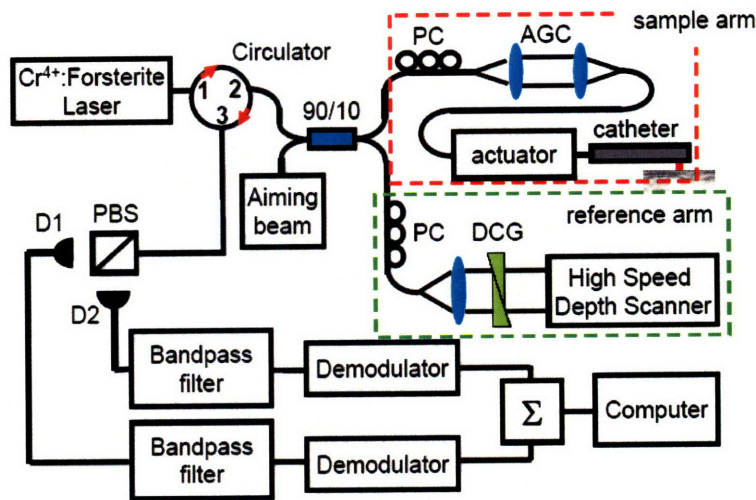


**Figure 3.** Schematic of endoscopic OCT system using broadband Cr<sup>4+</sup>:Forsterite light. Accurate dispersion matching is achieved with an air-gap coupling (AGC) and dispersion-compensating prisms (DCG); enabling broadband, high-resolution operation. High speed delay scanner enables real-time, *in vivo* imaging at 4 frames per second. Figure is modified slightly from [18].

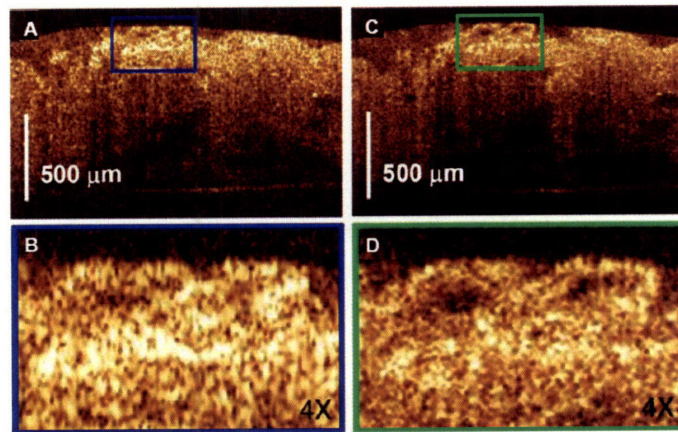


**Figure 4.** Comparison of ultrahigh and standard resolution OCT images of a biopsy specimen of Barrett's esophagus *ex vivo*. (A) Standard resolution OCT image with 4x enlargement in (B); (C) Ultrahigh resolution OCT image with 4x enlargement in (D). Ultrahigh resolution OCT image shows reduced speckle size and visualizes fine morphological features more clearly than standard resolution OCT. Figure is modified slightly from [19].

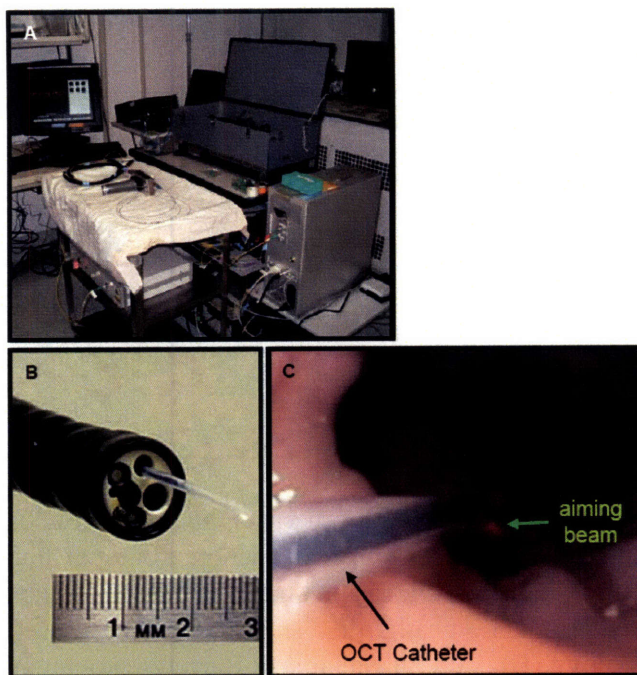


**Figure 5.** Photographs of (A) the endoscopic OCT system, (B) a fiber-optic imaging catheter in an endoscope working channel, and (C) an endoscopic view during the imaging procedure.

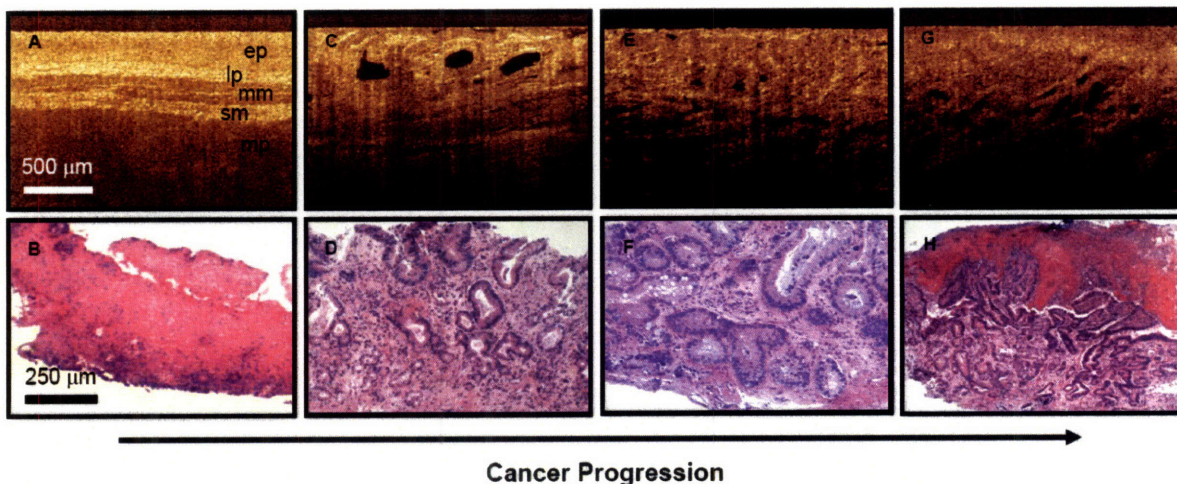


**Figure 6.** Ultrahigh resolution EOCT images of the human esophagus. (A) Normal squamous epithelium with a characteristic layered architecture. (C) Barrett's esophagus. The layered architecture is replaced by glandular structures. (E) High-grade dysplasia characterized by irregular, distorted, and cribriform or villiform glandular architecture and is more heterogeneous than non-dysplastic Barrett's epithelium. (G) Esophageal adeno-carcinoma with epithelial disruption and stromal infiltration extending from the superficially ulcerated carcinoma. (B, D, F, H) Corresponding pinch biopsy histology to OCT images (left). Figure is modified slightly from [19].

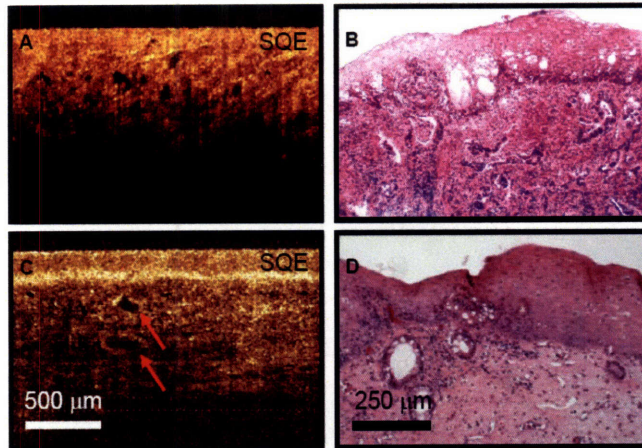


**Figure 7.** Ultrahigh resolution EOCCT can visualize the submucosa which cannot be seen with endoscopy. (A) Esophageal adeno-carcinoma underneath benign squamous epithelium. The EOCCT image shows irregularly shaped and crowded glandular architecture underneath the smooth squamous epithelium, later confirmed by histology (B). (C) Subsquamous Barrett's esophagus. OCT reveals squamous neo-epithelium similar to that observed from normal esophagus. However, glandular structures characteristic of Barrett's esophagus can be seen under the smooth-appearing epithelium. (D) is the corresponding histology. Figure is modified slightly from [19].

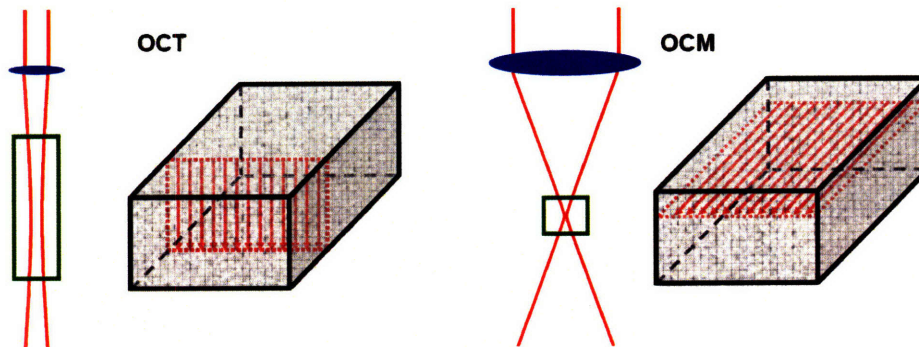


**Figure 8.** Schematic illustrating the main difference between OCT and OCM imaging. OCT systems operate with low numerical aperture optics to preserve transverse resolution over the whole imaging range. In contrast, OCM systems use high numerical aperture optics to provide small focal spot sizes, enabling cellular resolution imaging. The transverse resolution at the focal plane is much higher than OCT, but degrades rapidly at planes out of focus. Consequently, 2D raster scan which generates *en face* images is used in OCM as opposed to the depth priority scan used in OCT.

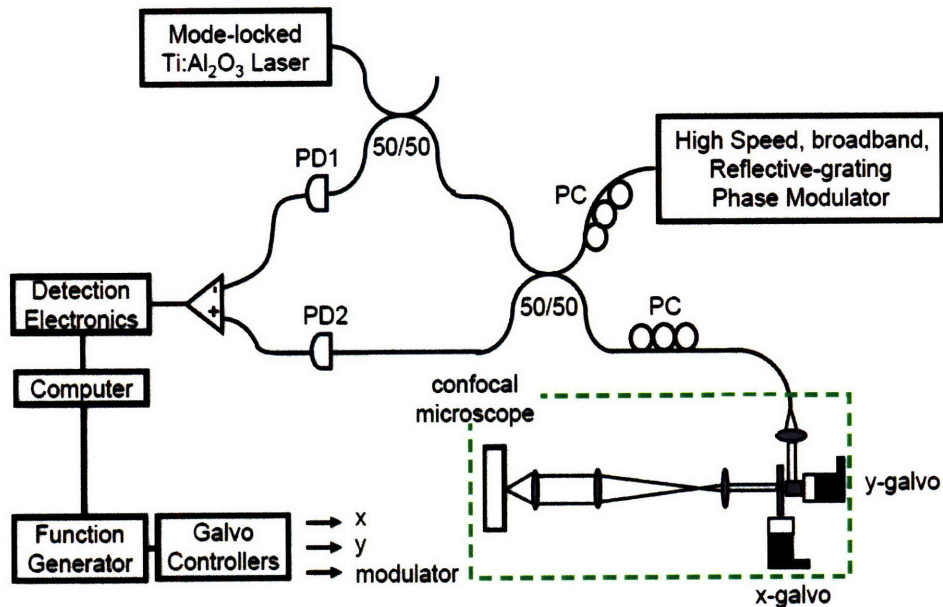


**Figure 9.** Schematic of the first high speed OCM system for *in vivo* cellular imaging. A high speed, dispersion-managed grating phase modulator was used in the reference arm to achieve real-time imaging. High-speed OCM attains cellular resolution images as a complement to high-speed OCT. Figure is modified slightly from [29].

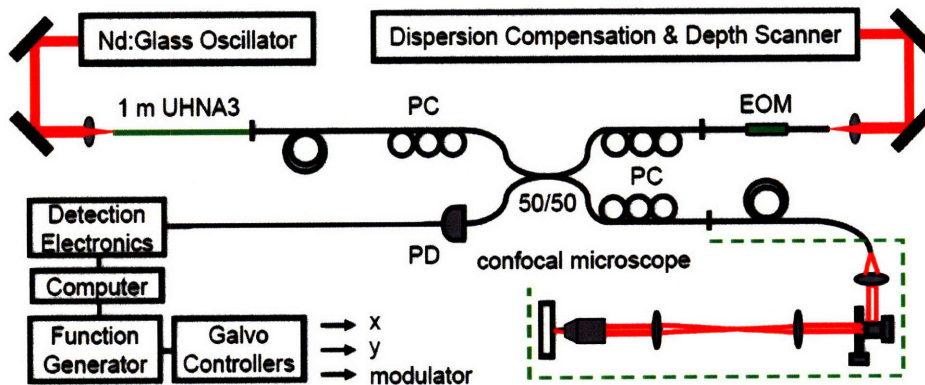


**Figure 10.** Schematic of the 2<sup>nd</sup> generation high-speed OCM imaging system. A 1 m length of high NA germanium-doped optical fiber (UHNA3) is used to broaden the spectrum from the oscillator and provide  $<4 \mu\text{m}$  axial resolution. The system operates at 1060 nm center wavelength using a broadband electro-optic waveguide phase modulator (EOM). Figure is modified slightly from [37].

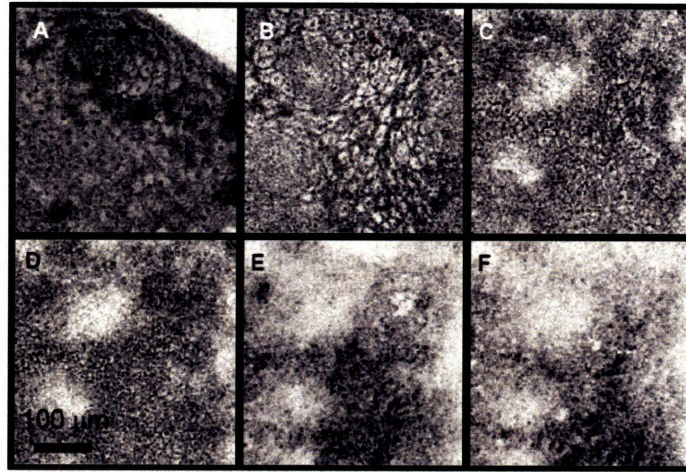


**Figure 11.** Progression of cellular architecture with depth in the stratified squamous epithelium of the esophagus. Image depths for (A) thru (F) are: 30, 90, 180, 210, 300, 330  $\mu\text{m}$ , respectively. Expected increase of nuclear-to-cytoplasm ratio with depth is apparent. The ability to identify changes in cell size, shape, and nuclear-to-cytoplasm ratio promises to improve differentiation of dysplasia and cancer. Figure is modified slightly from [37].

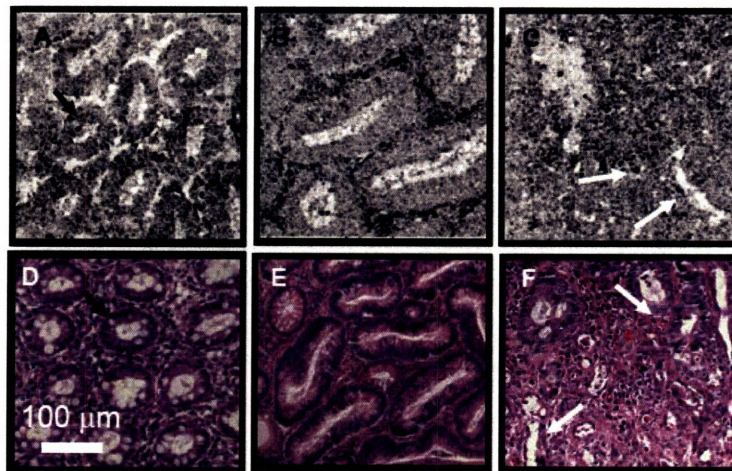


**Figure 12.** OCM visualizes differences between normal epithelium, dysplastic adenoma and adenocarcinoma in human colon *ex vivo*. (A) Normal epithelium. (B) Dysplastic adenoma. Crypt elongation and irregularity with hyper-scattering nuclei are apparent. (C) Adenocarcinoma. Loss of crypt organization, heterogeneous glands, and dense stroma can be clearly identified. D-F: Corresponding histology. Figure is modified slightly from [37].

## References

- [1] D. Huang, E. A. Swanson, C. P. Lin, J. S. Schuman, W. G. Stinson, W. Chang, M. R. Hee, T. Flotte, K. Gregory, C. A. Puliafito, and J. G. Fujimoto, "Optical Coherence Tomography," *Science*, vol. 254, pp. 1178-1181, Nov 1991.
- [2] J. G. Fujimoto, C. Pitris, S. A. Boppart, and M. E. Brezinski, "Optical coherence tomography: an emerging technology for biomedical imaging and optical biopsy," *Neoplasia*, vol. 2, pp. 9-25, Jan-Apr 2000.
- [3] J. G. Fujimoto, "Optical coherence tomography for ultrahigh resolution in vivo imaging," *Nature Biotechnology*, vol. 21, pp. 1361-1367, Nov 2003.
- [4] W. Drexler, U. Morgner, F. X. Kartner, C. Pitris, S. A. Boppart, X. D. Li, E. P. Ippen, and J. G. Fujimoto, "In vivo ultrahigh-resolution optical coherence tomography," *Optics Letters*, vol. 24, pp. 1221-1223, Sep 1999.
- [5] I. Hartl, X. D. Li, C. Chudoba, R. K. Hganta, T. H. Ko, J. G. Fujimoto, J. K. Ranka, and R. S. Windeler, "Ultrahigh-resolution optical coherence tomography using continuum generation in an air-silica microstructure optical fiber," *Optics Letters*, vol. 26, pp. 608-610, May 2001.
- [6] Y. Wang, Y. Zhao, J. S. Nelson, Z. Chen, and R. S. Windeler, "Ultrahigh-resolution optical coherence tomography by broadband continuum generation from a photonic crystal fiber," *Optics Letters*, vol. 28, pp. 182-184, Feb 2003.
- [7] K. Bizheva, B. Povazay, B. Hermann, H. Sattmann, W. Drexler, M. Mei, R. Holzwarth, T. Hoelzenbein, V. Wacheck, and H. Pehamberger, "Compact, broad-bandwidth fiber laser for sub-2-microm axial resolution optical coherence tomography in the 1300-nm wavelength region," *Optics Letters*, vol. 28, pp. 707-709, May 2003.
- [8] G. J. Tearney, M. E. Brezinski, B. E. Bouma, S. A. Boppart, C. Pitvis, J. F. Southern, and J. G. Fujimoto, "In vivo endoscopic optical biopsy with optical coherence tomography," *Science*, vol. 276, pp. 2037-2039, Jun 1997.
- [9] A. M. Sergeev, V. M. Gelikonov, G. V. Gelikonov, F. I. Feldchtein, R. V. Kuranov, N. D. Gladkova, N. M. Shakhova, L. B. Suopova, A. V. Shakhov, I. A. Kuznetzova, A. N. Denisenko, V. V. Pochinko, Y. P. Chumakov, and O. S. Streltsova, "In vivo endoscopic OCT imaging of precancer and cancer states of human mucosa," *Optics Express*, vol. 1, Dec 1997.
- [10] S. Jäckle, N. Gladkova, F. Feldchtein, A. Terentjeva, B. Brand, G. Gelikonov, V. Gelikonov, A. Sergeev, A. Fritscher-Ravens, J. Freund, U. Seitz, S. Schröder, and N. Soehendra, "In vivo endoscopic optical coherence tomography of esophagitis, Barrett's esophagus, and adenocarcinoma of the esophagus," *Endoscopy*, vol. 32, pp. 750-755, Oct 2000.

- [11] J. M. Ponerros, S. Brand, B. E. Bouma, G. J. Tearney, C. C. Compton, and N. S. Nishioka, "Diagnosis of specialized intestinal metaplasia by optical coherence tomography," *Gastroenterology*, vol. 120, pp. 7-12, Jan 2001.
- [12] J. A. Evans, J. M. Ponerros, B. E. Bouma, J. Bressner, E. F. Halpern, M. Shishkov, G. Y. Lauwers, M. Mino-Kenudson, N. S. Nishioka, and G. J. Tearney, "Optical coherence tomography to identify intramucosal carcinoma and high-grade dysplasia in Barrett's esophagus," *Clinical Gastroenterology and Hepatology*, vol. 4, pp. 38-43, Jan 2006.
- [13] A. M. Rollins, R. Ung-arunyawee, A. Chak, R. C. K. Wong, K. Kobayashi, M. V. Sivak, Jr., and J. A. Izatt, "Real-time in vivo imaging of human gastrointestinal ultrastructure by use of endoscopic optical coherence tomography with a novel efficient interferometer design," *Optics Letters*, vol. 24, pp. 1358-1360, Oct 1999.
- [14] S. Jäckle, N. Gladkova, F. Feldchtein, A. Terentieva, B. Brand, G. Gelikonov, V. Gelikonov, A. Sergeev, A. Fritscher-Ravens, J. Freund, U. Seitz, S. Soehendra, and N. Schrödern, "In vivo endoscopic optical coherence tomography of the human gastrointestinal tract--toward optical biopsy," *Endoscopy*, vol. 32, pp. 743-749, Oct 2000.
- [15] P. R. Pfau, M. V. Sivak, Jr., A. Chak, M. Kinnard, R. C. Wong, G. A. Isenberg, J. A. Izatt, A. Rollins, and V. Westphal, "Criteria for the diagnosis of dysplasia by endoscopic optical coherence tomography," *Gastrointest Endosc*, vol. 58, pp. 196-202, Aug 2003.
- [16] B. Shen, G. Zuccaro, Jr., T. L. Gramlich, N. Gladkova, P. Trolli, M. Kareta, C. P. Delaney, J. T. Connor, B. A. Lashner, C. L. Bevins, F. Feldchtein, F. H. Remzi, M. L. Bambrick, and V. W. Fazio, "In vivo colonoscopic optical coherence tomography for transmural inflammation in inflammatory bowel disease," *Clin Gastroenterol Hepatol*, vol. 2, pp. 1080-1087, Dec 2004.
- [17] L. Familiari, G. Strangio, P. Consolo, C. Luigiano, M. Bonica, G. Barresi, V. Barresi, P. Familiari, G. D'Arrigo, A. Alibrandi, A. Zirilli, W. Fries, and M. Scaffidi, "Optical coherence tomography evaluation of ulcerative colitis: The patterns and the comparison with histology," *American Journal of Gastroenterology*, vol. 101, pp. 2833-2840, Dec 2006.
- [18] P. R. Herz, Y. Chen, A. D. Aguirre, J. G. Fujimoto, H. Mashimo, J. Schmitt, A. Koski, J. Goodnow, and C. Petersen, "Ultrahigh resolution optical biopsy with endoscopic optical coherence tomography," *Optics Express*, vol. 12, pp. 3532-3542, Jul 26 2004.
- [19] Y. Chen, A. D. Aguirre, P. L. Hsiung, S. Desai, P. R. Herz, M. Pedrosa, Q. Huang, M. Figueiredo, S. W. Huang, A. Koski, J. M. Schmitt, J. G. Fujimoto, and H. Mashimo, "Ultrahigh resolution optical coherence tomography of Barrett's esophagus: preliminary descriptive clinical study correlating images with histology," *Endoscopy*, vol. 39, pp. 599-605, Jul 2007.
- [20] A. Hoffman, M. Goetz, M. Vieth, P. R. Galle, M. F. Neurath, and R. Kiesslich, "Confocal laser endomicroscopy: technical status and current indications," *Endoscopy*, vol. 38, pp. 1275-1283, Dec 2006.

- [21] R. Kiesslich, P. R. Galle, and M. F. Neurath, "Endoscopic surveillance in ulcerative colitis: Smart biopsies do it better," *Gastroenterology*, vol. 133, pp. 742-745, Sep 2007.
- [22] A. S. L. Kwan, C. Barry, I. L. McAllister, and I. Constable, "Fluorescein angiography and adverse drug reactions revisited: the Lions Eye experience," *Clinical and Experimental Ophthalmology*, vol. 34, pp. 33-38, Jan-Feb 2006.
- [23] Editorial, "Adverse effects of fluorescein angiography," *Acta Ophthalmologica Scandinavica*, vol. 84, pp. 720-721, 2006.
- [24] F. Musa, W. J. Muen, R. Hancock, and D. Clark, "Adverse effects of fluorescein angiography in hypertensive and elderly patients," *Acta Ophthalmologica Scandinavica*, vol. 84, pp. 740-742, Dec 2006.
- [25] R. Kiesslich, J. Burg, M. Vieth, J. Gnaendiger, M. Enders, P. Delaney, A. Polglase, W. McLaren, D. Janell, S. Thomas, B. Nafe, P. R. Galle, and M. F. Neurath, "Confocal laser endoscopy for diagnosing intraepithelial neoplasias and colorectal cancer in vivo," *Gastroenterology*, vol. 127, pp. 706-713, Sep 2004.
- [26] P. Delaney, S. Thomas, J. Allen, W. McLaren, E. Murr, and M. Harris, "Fluorescence confocal endomicroscopy in biological imaging," *Proceedings of SPIE*, vol. 6432, p. 64320G, 2007.
- [27] A. Osdoit, F. Lacombe, C. Cavé, S. Loiseau, and E. Peltier, "To see the unseeable: confocal miniprobes for routine microscopic imaging during endoscopy," *Proceedings of SPIE*, vol. 6432, p. 64320F, 2007.
- [28] J. A. Izatt, M. R. Hee, G. M. Owen, E. A. Swanson, and J. G. Fujimoto, "Optical coherence microscopy in scattering media," *Optics Letters*, vol. 19, pp. 590-592, Apr 1994.
- [29] A. D. Aguirre, P. Hsiung, T. H. Ko, I. Hartl, and J. G. Fujimoto, "High-resolution optical coherence microscopy for high-speed, *in vivo* cellular imaging," *Optics Letters*, vol. 28, November 2003.
- [30] S. Bourquin, A. D. Aguirre, I. Hartl, P. Hsiung, T. H. Ko, J. G. Fujimoto, T. A. Birks, W. J. Wadsworth, U. Bunting, and D. Kopf, "Ultrahigh resolution real time OCT imaging using a compact femtosecond Nd : Glass laser and nonlinear fiber," *Optics Express*, vol. 11, pp. 3290-3297, Dec 1 2003.
- [31] A. D. Aguirre, N. Nishizawa, J. G. Fujimoto, W. Seitz, M. Lederer, and D. Kopf, "Continuum generation in a novel photonic crystal fiber for ultrahigh resolution optical coherence tomography at 800 nm and 1300 nm," *Optics Express*, vol. 14, pp. 1145-1160, Feb 2006.
- [32] R. Huber, D. C. Adler, and J. G. Fujimoto, "Buffered Fourier domain mode locking: unidirectional swept laser sources for optical coherence tomography imaging at 370,000 lines/s," *Optics Letters*, vol. 31, pp. 2975-2977, Oct 2006.

- [33] A. Dubois, L. Vabre, A.-C. Boccara, and E. Beaurepaire, "High-resolution full-field optical coherence tomography with a Linnik microscope," *Applied Optics*, vol. 41, pp. 805-812, Feb 2002.
- [34] M. Akiba, K. P. Chan, and N. Tanno, "Full-field optical coherence tomography by two-dimensional heterodyne detection with a pair of CCD cameras," *Optics Letters*, vol. 28, pp. 816-818, May 2003.
- [35] A. Dubois, K. Grieve, G. Moneron, R. Lecaque, L. Vabre, and C. Boccara, "Ultra-high-resolution full-field optical coherence tomography," *Appl Opt*, vol. 43, pp. 2874-2883, May 2004.
- [36] W. Y. Oh, B. E. Bouma, N. Iftimia, S. H. Yun, R. Yelin, and G. J. Tearney, "Ultra-high-resolution full-field optical coherence microscopy using InGaAs camera," *Optics Express*, vol. 14, pp. 726-735, Jan 2006.
- [37] A. D. Aguirre, "Advances in Optical Coherence Tomography and Microscopy for Endoscopic Applications and Functional Neuroimaging," PhD thesis.

## CHAPTER 2 — Swept Source Optical Coherence Microscopy

### 2.1 Confocal Based Optical Coherence Microscopy

As described in chapter 1, OCM is a derivative of OCT which can improve the transverse resolution to achieve cellular level resolution. Swept source OCM, as well as time domain OCM, combines coherence-gated detection of OCT with fiber-based confocal microscopy to provide enhanced cellular resolution imaging in highly scattering tissues compared to confocal microscopy alone. Coherence-gated detection can also provide improved contrast compared to reflectance-based methods. The weakly backscattered signal is amplified optically by the heterodyne detection method.

Confocal based OCM has the unique advantage of using two distinct optical sectioning techniques – confocal gating and coherence gating. The confocal point spread function is entirely determined by the sample arm optics, and in particular, the numerical aperture of the final objective lens. The coherence gate, however, is determined by the light source bandwidth. The degree of confocal rejection of unfocused scattered light can be varied by changing the numerical aperture of the objective lens, while the amount of coherence gated sectioning can be varied by changing the bandwidth of the light source. The addition of high sensitivity coherence-gating to confocal detection not only strengthens the overall optical sectioning power but also makes it more robust to aberration and multiple scattering. It can extend the imaging depth in scattering media, providing an increase in imaging depth in scattering tissues of 30-50 % over confocal microscopy [1, 2].

The use of multiple optical sectioning techniques also allows considerable flexibility in system design for achieving high-resolution cellular images. In one limit, high NA optics can be used to produce very thin confocal tissue sections, while relatively weak coherence gating can be added to improve rejection of unwanted light. Figure 1 depicts the concept. The red curve is the point spread function of a fiber confocal microscope using a 1.3  $\mu\text{m}$  light source, SMF28 fiber, and 0.95 NA objective [3]. Due to the effect of finite aperture, the wing rises and lowers the image contrast. As shown by the black and blue curves, it is clear that adding the coherence gating helps reject the unwanted, out-of-focus scattered light.

In the other limit, broad bandwidth light sources as used in ultrahigh resolution OCT can

provide thin optical sectioning via coherence gating, and the confocal sectioning can be relaxed to facilitate development of miniaturized imaging devices. Figure 2 compares the confocal axial and transverse imaging resolution as a function of the numerical aperture of the probe optics to demonstrate this operating limit for OCM. A close inspection of confocal microscopy shows that the transverse resolution scales as  $1/NA$ , while axial resolution scales as  $1/NA^2$ , meaning that there exists a region of medium NA where the transverse resolution is sufficient for cellular imaging, but the axial resolution is not. Addition of a short coherence gate to provide extra axial sectioning can therefore make cellular imaging possible with much lower NA than is necessary for confocal microscopy alone.

## **2.2 High Speed Swept Source Optical Coherence Tomography**

Within the past 5 years there have been dramatic advances in OCT technology which enable 10 to 100 fold increases in imaging speed [4-6]. These advances greatly improve the performance of OCT and are key to enabling *in vivo* 3D-OCT. 3D-OCT promises to be a powerful imaging tool because three-dimensional volumetric data sets will enable virtual manipulation of tissue geometry for the visualization of structural morphology and improved processing techniques to reduce speckle and enhance contrast.

The key to recent advances in OCT imaging speed is the use of new OCT detection methods, known as Fourier-domain detection, that can achieve higher detection sensitivity by measuring backscattered light in the frequency domain [4-7]. Conventional OCT directly measures the interference signal, while Fourier-domain OCT measures the spectrum of the interference signal. The OCT axial scan is then constructed by Fourier transformation. While this requires spectral measurement and signal processing, it has the advantage that all of the echoes of light are measured simultaneously, rather than sequentially as in conventional OCT detection techniques. Several groups working independently demonstrated in 2003 that Fourier-domain detection enables 10 to 100 fold improvements in detection sensitivity, which enables corresponding improvement in the imaging speed [4-6].

Fourier-domain OCT can be performed using two complementary techniques, known as Spectral / Fourier-domain OCT [8-16] and swept source / Fourier-domain OCT [17-24]. Spectral / Fourier-domain detection uses a spectrometer and high speed, line scan camera to measure the interference spectrum. Spectral / Fourier-domain OCT typically operates at 800 nm

wavelengths with 29 kHz - 75 kHz axial scan rates [9, 10]. This technology has had a powerful impact on ophthalmic OCT imaging because it enables ultrahigh resolutions as well as 3D-OCT imaging of retinal pathologies [14-16]. In contrast, swept source / Fourier-domain OCT uses a frequency-swept laser light source and a photodetector to measure the interference spectrum. Figure 3 illustrates swept source / Fourier-domain detection. Frequency swept light that is backscattered from the sample is interfered with light that travels a fixed reference path delay. The intensity output of the interferometer oscillates at a beat frequency which is related to the path difference. Axial scan measurements of backscattering versus delay are measured by Fourier transforming the interferometer output. Swept source / Fourier-domain OCT technology has the advantage that it can perform imaging at longer wavelengths of 1000 nm and 1300 nm. Imaging at these wavelengths is important because it reduces optical scattering and improves image penetration depths [25]. Swept source OCT was first demonstrated in 1997 [17, 18], but high speed imaging with an axial scan rate exceeding 10 kHz was not demonstrated until 2003 by Yun *et al.* [20]. Lately, Huber *et al.* developed a new class of frequency-swept laser source and further pushed the axial scan rates to 370 kHz, ~100 times faster than standard OCT [24].

### 2.3 Fourier-domain Mode-locked Lasers

Frequency swept laser light sources are a key technology for swept source / Fourier-domain OCT. The laser sweep rate and tuning range determine the OCT imaging axial scan rate and axial resolution, respectively. Previously, swept lasers using a tunable filter with a diffraction grating and rotating polygon mirror achieved sweep rates of 15.7-115 kHz [20, 22]. Our group recently developed a new frequency swept laser technology, known as Fourier-domain modelocking (FDML), that overcomes fundamental limitations in sweep rate present in conventional swept lasers, enabling record OCT imaging speeds and performance [23, 24]. Higher acquisition speed enables increased field of view, high volumetric sampling densities, and reduced motion artifacts to enable *in vivo* 3D-OCT imaging.

Figure 4 shows a schematic of an FDML laser. The laser consists of a long optical fiber, a semiconductor optical amplifier (SOA) gain element, a tunable filter (fiber Fabry-Perot tunable filter FFP-TF) and optical isolators to produce unidirectional operation. The length of the optical fiber, typically 1 to 5 km coiled on a compact spool, determines the roundtrip propagation time of the light. The laser output is extracted using an optical fiber coupler. FDML lasers are

compact, robust, contain no free-space components, and are significantly lower cost than femtosecond lasers. FDML lasers achieve improved performance compared to conventional swept lasers by synchronizing the sweep rate of the tunable filter to the roundtrip time of the light in the laser. The tunable filter is driven through one tuning cycle in exactly the same time it takes for the light to travel once around the cavity. Each frequency within the sweep is then transmitted again by the tunable filter. This occurs repetitively such that the entire sweep is essentially stored in the laser. The laser light at different frequencies does not have to build up from background emission, as in conventional frequency swept lasers [26] and therefore the tuning rate can be increased without sacrificing performance. This synchronous operation gives FDML lasers excellent stability and noise performance and enables high sweep rates over broad tuning ranges with high output powers.

## 2.4 Swept Source Optical Coherence Microscopy

In this chapter, we demonstrate a novel OCM system which uses swept source / Fourier-domain detection, termed swept source OCM. The method is, in essence, swept source OCT with high numerical aperture optics. As such, it provides full three-dimensional volume acquisition within the confocal gate, which will allow multiple *en face* sections to be taken around the focal plane. The volumetric scan should make possible new approaches to compensate for shifts between the confocal and coherence gate and may enable volumetric as well as single slice cellular imaging. Since the technique shares the same principle as 3D-OCT, it will also facilitate combined, state-of-art OCT and OCM imaging systems. Compared with previous implementations of time-domain OCM, swept-source OCM offers simplification in reference arm optical design at the expense of increased complexity in the detection electronics and the need for increased computing power.

### 2.4.1. Motivations

Traditionally, OCM is implemented with time domain detection, which allows high speed *en face* imaging in order to eliminate motion artifacts [27-30]. However, time domain systems have a number of features that make the optical system complex. First, a rapid phase modulation scheme in the reference arm is required. Several methods have been proposed, including rapid scanning optical delay lines [29], electro-optic modulators [31, 32], and acousto-optic

modulators [33, 34]. All methods require sophisticated optical designs and specific issues, like dispersion compensation and polarization control need to be carefully addressed. Second, coordination between the coherence gate and confocal gate is critical to ensure optimal image quality in highly scattered tissues. Due to the inhomogeneous nature of tissues, the matching between the two gates generally can not be set *a priori* without real time measurement. In addition, when a fiber based endoscope system is used, any unintentional stretch or stress to the fiber can introduce gate mismatch and degrade the image quality. Therefore, a feedback loop and a fast coordination algorithm are required to maintain optimal image quality during the imaging period. Finally, due to the limited field of view, usually a few hundred  $\mu\text{m}$ , OCM itself can suffer from sampling error in clinical studies. One solution to this limitation is to use OCT for large scale survey and to conduct OCM only in the regions where abnormalities are detected using OCT. An imaging modality which incorporates high speed OCT and OCM is thus desirable.

Recent work has shown that spectral / Fourier-domain detection enables OCT imaging with dramatically improved speed and sensitivity over conventional time domain detection [4-6]. Spectral / Fourier-domain OCM has also been investigated [35-37]. Different from time domain OCM, which acquires only a single *en face* image, spectral / Fourier-domain OCM generates an image by acquiring an entire 3D volume and rendering the *en face* plane. OCM and OCT using spectral / Fourier-domain detection has the advantage of sharing the same optics in the reference arm, which makes integration of the two techniques relatively straightforward. In addition, spectral / Fourier-domain detection measures optical signals from all depths simultaneously and therefore the need for coherence and confocal gate coordination is significantly relaxed. An *en face* OCM image at a depth matched to the confocal gate can be digitally extracted from the entire 3D dataset. Similarly, a confocal image with reduced speckle can be generated by summing the dataset in the axial direction.

Swept source / Fourier-domain detection has similar advantages to spectral / Fourier-domain detection, but does not require a spectrometer and line scan camera and therefore has higher detection efficiency and higher imaging speed. As mentioned in section 2.3, FDML lasers are especially promising for high speed OCT imaging [23, 24]. Axial scan rates up to 370 kHz have been demonstrated [24] and could provide OCM frame rates of  $>4$  Hz with  $300 \times 300$  pixels, which is comparable to high-speed time domain OCM and is sufficient to eliminate motion

artifacts for *in vivo* imaging.

#### 2.4.2. System setup and characterization

The FDML laser used in the study has an axial scan rate of 42 kHz, a bandwidth of  $\sim 90$  nm centered at 1290 nm and an output power of  $\sim 12$  mW. Figure 5A is the spectrum of the laser and figure 5B shows the measured axial point spread function on a log scale at the depth of  $\sim 450$   $\mu\text{m}$ , which is typically the deepest penetration depth of the OCM system while preserving reasonable image quality in highly scattered tissues. The dynamic range is higher than 50 dB within this depth range. Different from time domain system, dynamic range is as important as sensitivity a parameter for swept source OCM system performance evaluation. Since light backscattered from all axial positions of the sample is detected simultaneously in Fourier-domain techniques, cross-talk between signals from different depths can occur. When there is a strong signal at a given depth, amplitude noise from the light source generates noise in the fringe signals, which then generates an elevated noise floor over the entire scan range [24]. When superficial structure is of interest, carefully tilting the sample to minimize the specular reflection is then necessary.

Figure 6 is a schematic diagram of the swept source OCM system. 3% of the laser power is coupled to an optical spectrum analyzer (OSA) for monitoring the spectrum and a Mach-Zehnder interferometer for recalibration of time to optical frequency. The recalibration is necessary because the FDML laser does not sweep linearly in frequency. The other 97% of the laser power is then split equally and delivered to a reference arm and a sample arm. A polarization controller and a neutral density filter wheel are used to set the reference arm power to obtain the optimum sensitivity performance. Although the types of glasses in the objective lens are unknown, the dispersion in the sample arm is partially balanced in the reference arm by use of SFL6 and can be compensated numerically as described in reference [13]. The sample arm has a scanning confocal microscope with a pair of closely spaced galvanometer-driven mirrors (Cambridge Technology, Model 6210 Optical Scanner with 3mm aperture protected silver mirror), a pair of relay lenses (Thorlabs achromats,  $f_1 = 75\text{mm}$ ,  $f_2 = 100\text{mm}$ ), and a 63X water-immersion objective (Olympus, Achromplan, Infinity corrected, NA=0.9, WD=2.0 mm). Of note, the objective has high loss of 55% at this wavelength and the incident power on the sample is reduced to 1.5 mW. The measured sensitivity is higher than 98 dB. The back aperture of the objective is intentionally underfilled such that the effective NA is  $\sim 0.35$ . This provides a good compromise

between transverse resolution and depth of field, such that a series of high quality, coherence gated *en face* images can be extracted from the 3D dataset. The excess laser noise is cancelled by dual-balanced detection. The control software is developed in Labview with the processing core developed in C.

The confocal gate is measured to be  $\sim 20 \mu\text{m}$  (red line in Figure 7A) by blocking the reference arm and recording the dc photodetector signal while translating a mirror in the sample arm around the focus. The confocal gate is asymmetric, suggesting that the objective lens still has achromatic aberration. The coherence gate is measured to be  $\sim 8 \mu\text{m}$  (black line in Figure 5A), which is slightly larger than the theoretical value and is the result of the non-Gaussian spectral shape, nonlinear sweep speed, and the frequency calibration errors as described in reference [23].

Figure 7B shows the transverse resolution and the field-of-view of the microscope system. The smallest elements measuring  $2.2 \mu\text{m}$  in width on the USAF 1951 resolution target can be clearly visualized. The  $e^{-2}$  radius was estimated to be  $1.6$  to  $1.8 \mu\text{m}$  over a  $220 \mu\text{m} \times 220 \mu\text{m}$  field-of-view using an edge-scan measurement method [38]. The field-of-view is about 20% smaller than expected due to the close-coupled scan design. To obtain a symmetric field-of-view, center of the scanner pair is imaged onto the pupil plane, leading to imperfect pivot for both axes. With the pivot error, the beam clips on the limiting aperture of the objective and vignetting effect limits the field-of-view to a smaller value.

#### 2.4.3. Imaging results

All OCM images presented in this chapter are white-on-black and in linear scale. Figure 8A shows an *in vivo* volumetric image of a *Xenopus laevis* tadpole, a commonly used model organism in developmental biology specimens. The 3D dataset is post-processed to generate a series of *en face* images at different depths near the focal plane. Three representative *en face* images  $\sim 12 \mu\text{m}$  apart in depth are shown in Figure 8B, 8C, and 8D. Degradation of transverse resolution from image C to D is apparent due to the finite depth of field with  $\sim 0.35$  NA. The ability to generate images at different depths covering the entire focal range within one acquisition circumvents the need of online coordination between coherence gate and confocal gate. In contrast, for time domain OCM, only one *en face* image is acquired at a time and therefore precise control of the position of the coherence gate is required to ensure optimal image

quality. Figure 9 is a cartoon which demonstrates the concept.

Figure 10 presents additional *in vivo* cellular images of a *Xenopus laevis* tadpole. Images A and C are two *en face* images acquired when the focus is set at  $\sim 200\ \mu\text{m}$  and  $\sim 400\ \mu\text{m}$  below the surface. Image size is  $256 \times 256$  pixels over the field of view of  $\sim 220\ \mu\text{m} \times 220\ \mu\text{m}$ . Nuclei and cell membranes can be clearly visualized in both images. Cytoskeletons can also be identified in image C. Images B and D are generated by summing the 3D dataset in the axial direction. Because the coherence gate is shorter than the confocal gate in this study, the images resemble those taken by a confocal microscope, but with reduced speckle. In contrast to standard confocal microscopy, these images were acquired using a relatively low NA and long confocal gate. Obscuration of detailed cellular structures and loss of contrast are evident, indicative of the insufficient rejection of out-of-focus scattered light by the confocal gate alone. Figure 11 shows swept source OCM images and H&E stained histology of a fixed rat kidney, demonstrating the capability to image in highly scattered biological samples. Images A and B are acquired when the focus is at  $\sim 40\ \mu\text{m}$  and  $\sim 120\ \mu\text{m}$  below the surface, respectively. The cell lining along the kidney tubules is readily visible and small regions of bright reflectivity, consistent with nuclei, can also be observed in the images.

The ability to generate high quality cellular images in human tissue with the system is demonstrated in Figure 12. Image A is a swept source OCM image of a normal human colonic mucosa taken at  $\sim 100\ \mu\text{m}$  below the surface while image B is H&E stained histology. The sample was preserved in phosphate-buffered saline (PBS) and imaged within  $\sim 6$  hours of excision, then fixed and processed for histology. Normal colonic mucosa shows the presence of round crypts with goblet cells inside epithelium lining the lumen. In addition, the lamina propria houses many lymphoid cells. All features mentioned above can be clearly resolved in the swept source OCM image. Figures 12C and 12D are images of a different region at  $\sim 100\ \mu\text{m}$  and  $\sim 150\ \mu\text{m}$  below the surface, respectively. A decrease of lumen size over depth is apparent and detailed structures like goblet cells and lymphoid cells can still be easily identified deep in the tissue.

Figure 13 presents a series of confocal as well as OCM images in fixed rat kidney acquired when the focus is at  $\sim 40\ \mu\text{m}$ ,  $\sim 80\ \mu\text{m}$ , and  $\sim 120\ \mu\text{m}$  below the surface. The addition of the coherence gating helps reject the unwanted, out-of-focus scattered light and hence the image contrast in OCM images is higher and cellular details can be delineated more clearly. Figure 14 presents a series of confocal as well as OCM images in human colon *ex vivo* acquired at different

focal depths. At each focal depth, a series of OCM images with different path length differences from the focus are shown. Degradation of transverse resolution with path length differences is apparent due to the finite depth of field with  $\sim 0.35$  NA focusing. The ability to generate images at different depths covering the entire focal range within one acquisition circumvents the need of online coordination between coherence gate and confocal gate. Figure 14 also suggests that the quality of confocal gated images degrades much faster than coherence gated images as a function of focal depth, which is a consequence of coherence gate's better resistance to aberration and multiple scattering.

In summary, the feasibility of swept source OCM using a FDML laser is demonstrated. 3D cellular imaging is presented in *Xenopus laevis* tadpoles, rat kidney, and human colon with resolution of  $1.6 \mu\text{m} \times 8 \mu\text{m}$  (transverse  $\times$  axial),  $220 \mu\text{m} \times 220 \mu\text{m}$  field of view, and sensitivity higher than 98 dB. The imaging speed is currently limited at  $\sim 0.7$  fps by the data acquisition and processing hardware, but has the potential to be significantly increased, enabling *in vivo* imaging and real-time display. To fully utilize the laser's high sweep rate and dynamically display an *en face* image of interest, an analog demodulation scheme should be developed so that the digital processing requirements can be minimized. Unfortunately because of the nonlinear frequency sweep of the FDML laser, a simple band-pass filter is not sufficient to demodulate a particular *en face* image from the 3D dataset. However, matched filter approaches should be possible and promise to enable very high demodulation speeds. Toward improving resolution, we have recently developed FDML lasers with tuning ranges of  $\sim 170$  nm using specially matched SOAs. This suggests that axial resolutions can be improved to  $\sim 5 \mu\text{m}$ , which is comparable to the thickness of standard histological sections.

#### **2.4.4. Discussion and Summary**

Swept source / Fourier-domain OCM has several advantages compared to time domain OCM. First, it more easily enables integration with high speed OCT. An imaging modality which can be easily switched between high speed OCT for large scale survey imaging and OCM for a detailed cellular level examination would be a powerful modality for optical biopsy and facilitate clinical studies. Second, coordination of the confocal and coherence gates is not necessary since a stack of coherence-gated images which cover the entire focal range is acquired simultaneously. Swept source / Fourier-domain OCM also has the advantage of reduced system complexity. Rapid phase modulators in time domain OCM system and spectrometers in spectral / Fourier-

domain OCM are not required in swept source / Fourier-domain OCM. Importantly, and in contrast to OCT, there is no inherent sensitivity advantage of Fourier-domain OCM compared to time domain OCM. The extremely high data rates necessary to acquire an entire volume with Fourier-domain OCM result in reduction of pixel exposure / dwell time for any given pixel in the *en face* image, which effectively negates the sensitivity advantage.

Although the data rate of Fourier-domain OCM is higher than time domain OCM, the frame rate for an *en face* image at a particular depth is limited either by the camera readout rate or the laser sweep rate respectively. Unlike standard swept laser sources, the FDML laser can operate at extremely high speeds and therefore enables high speed, swept source / Fourier-domain OCM. FDML lasers overcome limitations of sweep speeds which are present in standard swept lasers and unprecedented high sweep rates up to 370 kHz have been demonstrated with a buffered configuration. At these speeds, >4 Hz frame rate can be supported and motion artifacts for *in vivo* imaging can be minimized. However, the high data rates of 3D volumetric imaging require advanced high-speed data processing solutions in order to perform real-time display. In terms of realtime processing and display, time domain OCM approaches are therefore currently easier to implement.

## **2.5 Analog Demodulation Scheme for Real-time Display**

As mentioned in the previous section, the current swept source OCM system lacks real-time display. The problem mainly comes from the fact that FDML laser has a nonlinear sweep in frequency. As described in section 3 and depicted in figure 3, there is a unique correspondence between path difference and interferometric signal beat frequency if the laser sweeps linearly in frequency. In that case, an analog band-pass filter is sufficient to demodulate a particular *en face* image from the 3D dataset.

There are two causes for the nonlinear sweep. First, in order to maximize the sweep rate, a sinusoidal waveform is used to drive the FFP filter. Second, it is the wavelength that changes linearly with the etalon spacing, not the frequency. Therefore, we still have nonlinear frequency sweep even if the driving waveform for the FFP filter is linear. Figure 15 shows a typical interferometric signal with a single reflector. Due to the nonlinear sweep, the beat frequency changes as a function of time and hence it no longer has one-to-one correspondence with the path difference. Nevertheless, a close inspection reveals that zero beat frequency is unique because it can only be generated when there is no path difference. A low-pass filter can thus do a good job

to extract the *en face* image from the plane whose path length matches that of the reference arm.

Working around the zero beat frequency, however, is susceptible to noises such as  $1/f$  detector noise. A way to circumvent the problem is to take advantage of the recalibration interferometer. Figure 16 is a suggested schematic of a dual interferometer setup with a common reference arm. Here a Michelson, instead of a Mach-Zehnder, interferometer is used as the recalibration interferometer (interferometer A) because the dispersion compensation is easier. Two independent interferometers can also be used, but the path length of the two reference arms has to be matched experimentally first. After the dual interferometer imaging system is built, one sets the sample arm of the recalibration interferometer such that a few MHz beat signal is generated. The beat frequency can be adjusted to minimize the noise. Now, mixing the detector outputs from both interferometers will generate a low-frequency beat signal which is related to the path difference between the two sample arms. Because the imaging system has a common reference arm (or the reference arm path length of the two independent interferometers is matched), a zero beat frequency is generated when the path length of the two sample arms matches. A low-pass filter then follows to extract the *en face* image from the plane whose path length matches that of the recalibration interferometer's sample arm. Of note, the zero beat frequency is generated at the mixer, not the detector, and therefore the noise problem is circumvented. Scanning the sample arm of the recalibration interferometer is equivalent to extracting *en face* images from different depths.

Figure 17 shows schematics of two possible demodulation electronics. Figure 17A starts with a typical IQ demodulator which is commonly used in communication to extract the envelope signal from a carrier amplitude modulated wave. It will be shown later that an IQ demodulator, which requires an additional mixer and a phase shifter to mix in quadrature, is necessary. An integrator then follows to get the amplitude of the envelope signal. Figure 17B is a simplified demodulation electronics. The low-pass filter is replaced directly by an integrator.

Figure 18 is the point spread function simulated by using a mirror as the sample and moving it along the axial axis. Demodulation electronics depicted in figure 17B is assumed in the simulation. The addition of an IQ demodulator removes most of the phase dependence except some superimposed zigzag patterns. The zigzag pattern comes from the fact that perfect  $\pi/2$  phase shifter required in the IQ demodulator is not feasible because the frequency of the interferometric signal changes over time. Of note, the two detector outputs always remain phase

locked because they are referenced to each other, given that the dispersion is perfectly compensated, and hence it seems that the IQ demodulator is not necessary at the first glance. Phase drift caused by path length fluctuation is still possible, but is accompanied by beat frequency shift in the swept source system. Due to the limited spectral resolution, a small beat frequency shift can not be detected and therefore the phase dependence of the point spread function shows up. Figure 19 shows another artifact coming from the proposed demodulation method. Due to mixing of two interferometric signals, the spectral bandwidth is effectively reduced by a factor of  $\sqrt{2}$  and the point spread function is widened accordingly. Nevertheless, it is much better than just using an analog band-pass filter, which is represented by the blue curve, and should be good enough for the purpose of real-time display.

Another interesting application of the proposed demodulation scheme is the real-time display of an arbitrary plane within the 3D volumetric dataset acquired by the high speed swept-source OCT. When the scanning of the recalibration interferometer's sample arm is synchronized with the 2D raster scanning, a target plane can be selected by adjusting the ratio of the scanning speeds.

## **Acknowledgements**

The contributions of several individuals to this chapter must be mentioned. All the fresh excised human tissues are provided by Dr. James Connolly from the Beth Israel Deaconess Medical Center. Former Post-doctoral associate Robert Huber and graduate student Desmond Adler developed the FDML laser for the study. Former graduate student Aaron Aguirre helped design the system and analyze the data.

## Figures

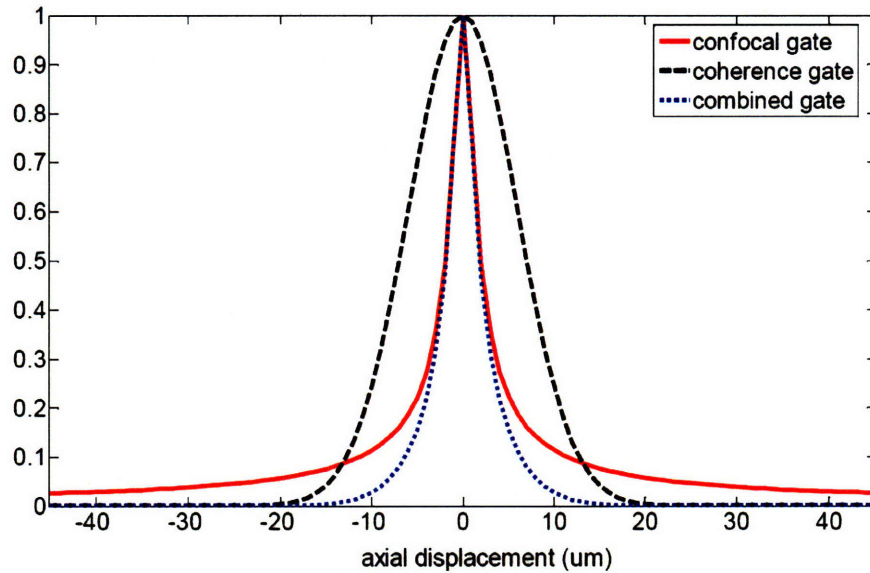


**Figure 1.** Axial point spread function of a confocal based optical coherence microscope. The confocal gate is calculated assuming a 1.3  $\mu\text{m}$  light source, SMF28 fiber, and 0.95 NA objective are used. High NA optics can be used to produce very thin confocal tissue sections, while relatively weak coherence gating can be added to improve rejection of unwanted light.

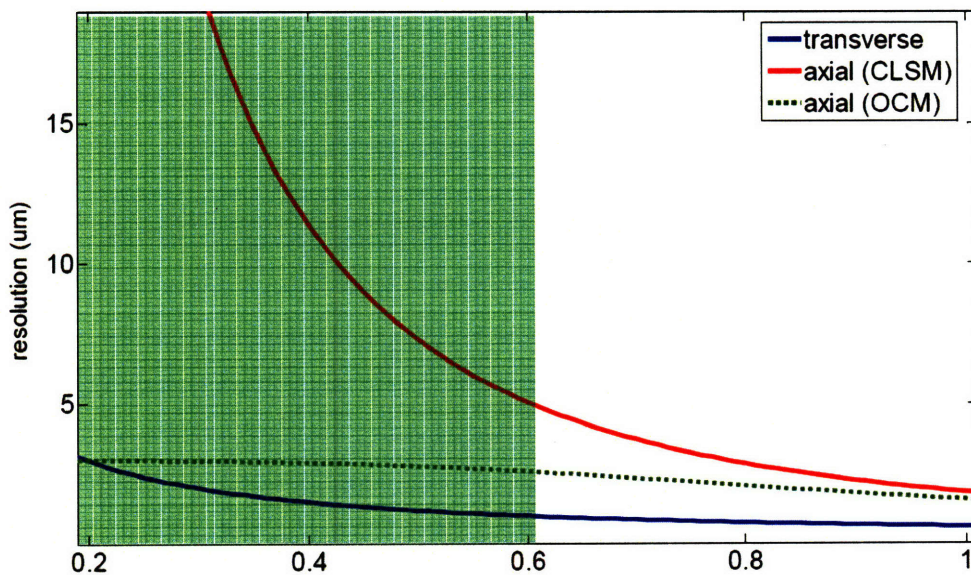


**Figure 2.** Optical resolutions with respect to the objective's NA. The transverse resolution of a standard confocal microscope scales as  $1/\text{NA}$  while axial resolution scales as  $1/\text{NA}^2$  and so there is a region of medium NA where the transverse resolution is sufficient for cellular imaging but the axial resolution is not. Addition of a short coherence gate to provide extra axial sectioning can therefore make cellular imaging possible in this regime.

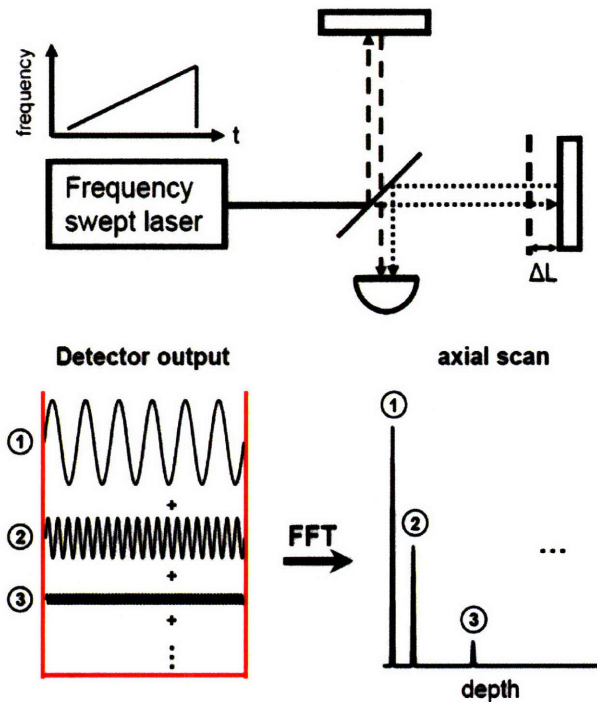


**Figure 3.** Principle of swept source / Fourier-domain OCT. Frequency swept light that is backscattered from the sample is interfered with light that travels a fixed reference path delay. The intensity output of the interferometer oscillates at a beat frequency which is related to the path difference. Axial scan measurements of backscattering versus delay are measured by Fourier transforming the interferometer output.

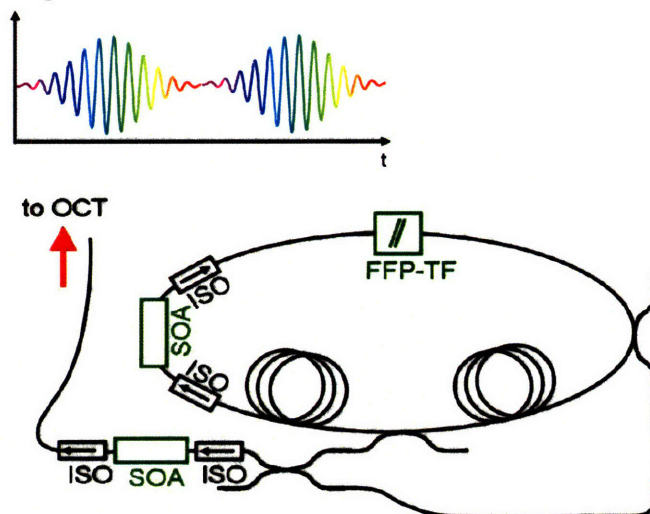


**Figure 4.** Schematic of a Fourier-domain mode-locked (FDML) laser. The laser has a long fiber and a tunable filter which is synchronized to the optical roundtrip time of light in the cavity. This synchronous operation gives FDML lasers excellent stability and noise performance and enables high sweep rates over broad tuning ranges with high output powers. Figure is modified slightly from [39].

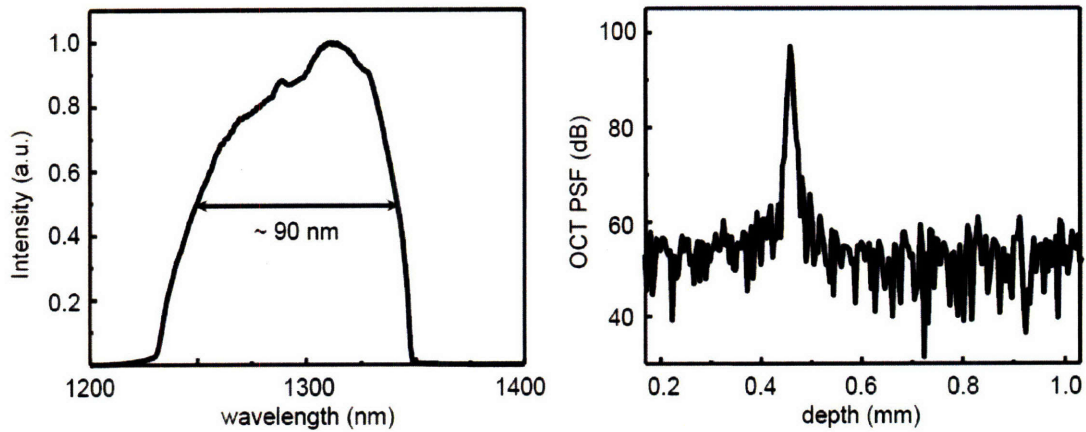


**Figure 5.** FDML laser characterization. (A) Spectrum of the laser. (B) Axial point spread function supported by the laser. The dynamic range is higher than 50 dB. Figure is modified slightly from [40].

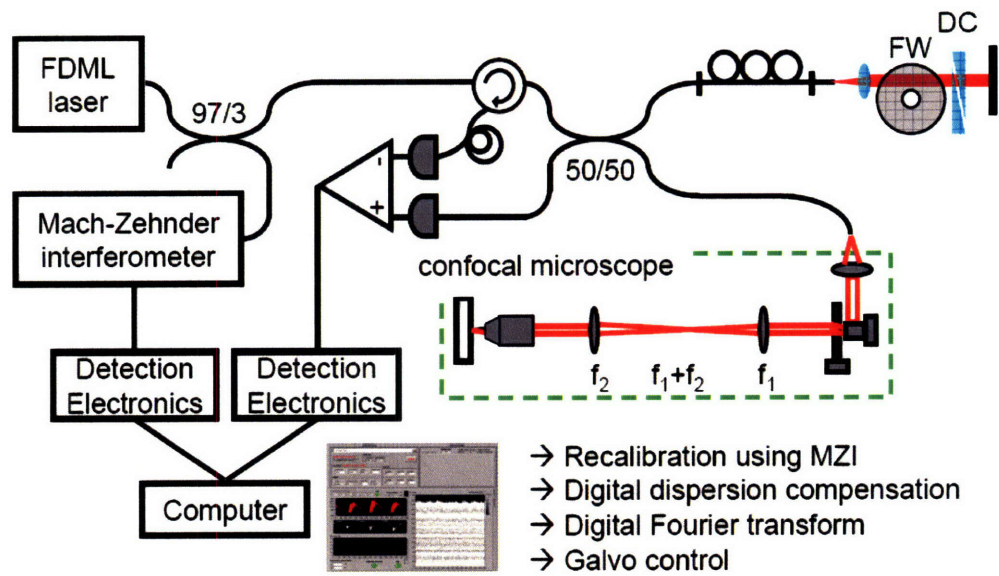


**Figure 6.** Schematic of the swept source OCM system. FW, neutral density filter wheel; DC, dispersion compensating glass. Swept source OCM acquires multiple *en face* planes and provides a platform for integrating OCT and OCM into a single instrument. Figure is modified slightly from [40].

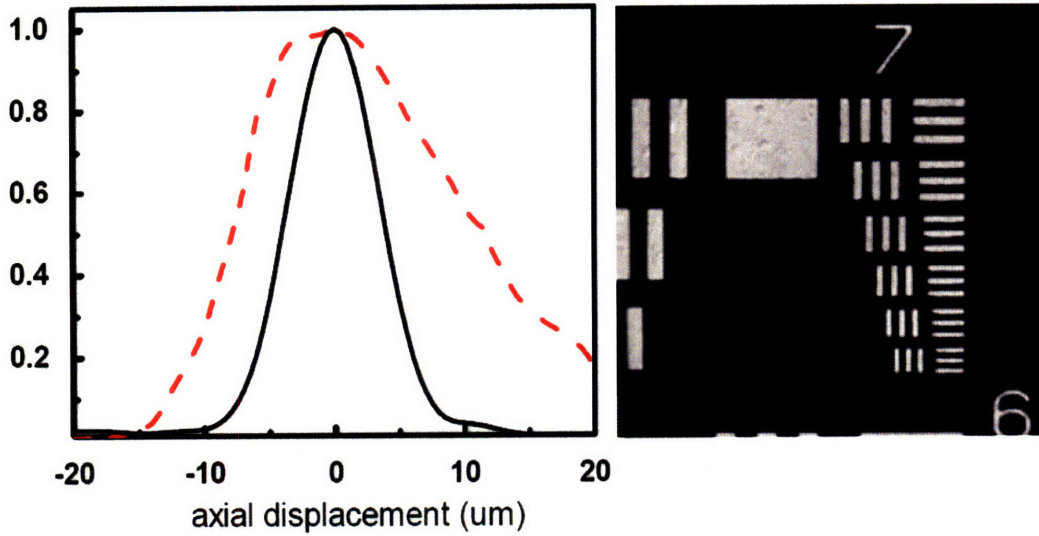


**Figure 7.** Swept source OCM system characterization. (A) The confocal gate (red line) and the coherence gate (black line) are measured to be  $\sim 20 \mu\text{m}$  and  $\sim 8 \mu\text{m}$ , respectively. (B) Transverse resolution is estimated to be  $\sim 1.6 \mu\text{m}$  and the smallest elements on the USAF resolution chart can be clearly resolved. Figure is modified slightly from [40].

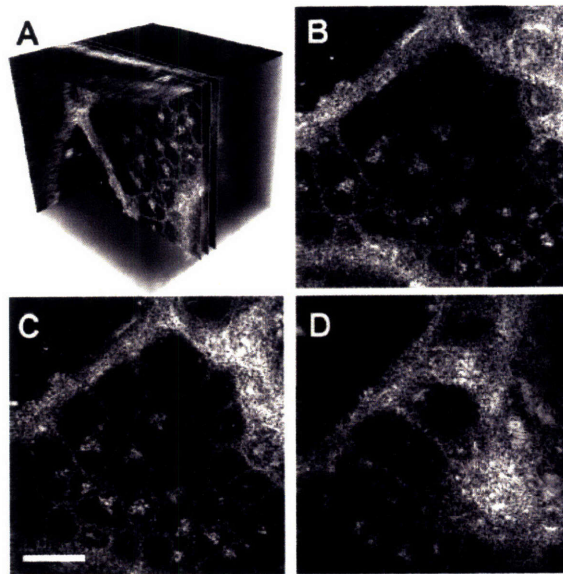


**Figure 8.** Extraction of *en face* images from the 3D dataset. (A) A volumetric image acquired by the swept source OCM system in  $\sim 1.5$  second. A series of *en face* images can then be extracted from the volume digitally. The volume size is  $\sim 220 \mu\text{m} \times 220 \mu\text{m} \times 220 \mu\text{m}$ . B-D: Three representative *en face* images  $\sim 12 \mu\text{m}$  apart in depth extracted from the volume around the focus. Scale bar:  $50 \mu\text{m}$ . Figure is modified slightly from [40].

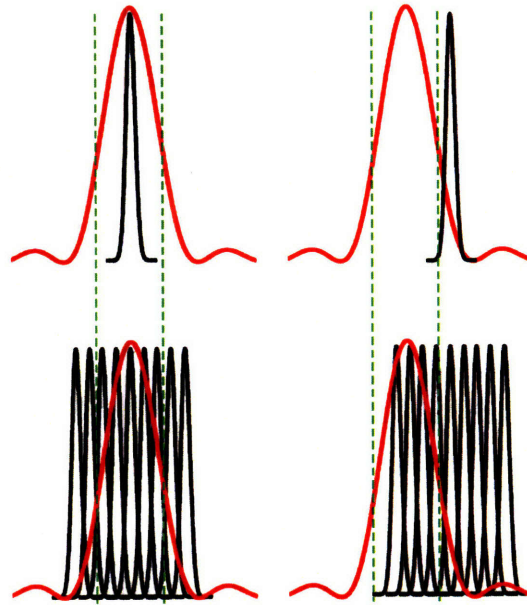


**Figure 9.** Cartoon showing that online coordination between coherence gate (black curve) and confocal gate (red curve) is not necessary for swept source OCM. (A) Time-domain OCM operates when the two gates are matched within a certain range represented by the dashed green curve. However, there are times that the two gates become mismatched due to index mismatch or unintentional fiber stretch and the image quality is degraded. (B) Swept source OCM acquires signals from all depths covering the entire focal range simultaneously and therefore the need for coherence and confocal gate coordination is relaxed.

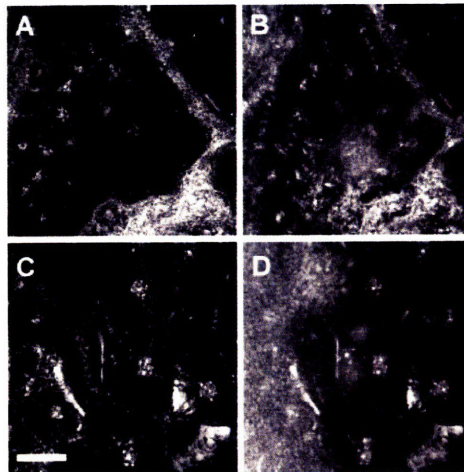


**Figure 10.** *In vivo* cellular images of a *Xenopus laevis* tadpole. (A) and (C) are OCM images at  $\sim 200 \mu\text{m}$  and  $\sim 400 \mu\text{m}$  below the surface, respectively. (B) and (D) are confocal-like images generated by summing the 3D datasets in the axial direction. Obscuration of detailed cellular structures and loss of contrast in the confocal-like images are evident. Scale bar:  $50 \mu\text{m}$ . Figure is modified slightly from [40].

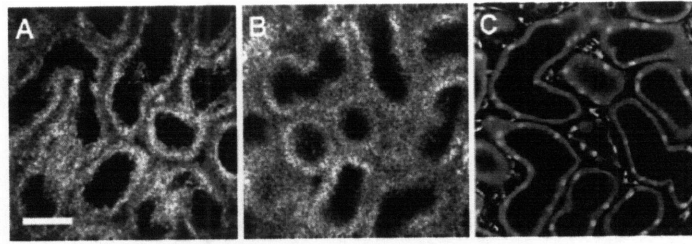


**Figure 11.** Cellular images of a fixed rat kidney. (A) and (B) are OCM images at  $\sim 40 \mu\text{m}$  and  $\sim 120 \mu\text{m}$  below the surface, respectively. (C) Representative histology stained with H&E. The cell lining along the kidney tubules and nuclei can be observed. Scale bar:  $50 \mu\text{m}$ . Figure is modified slightly from [40].

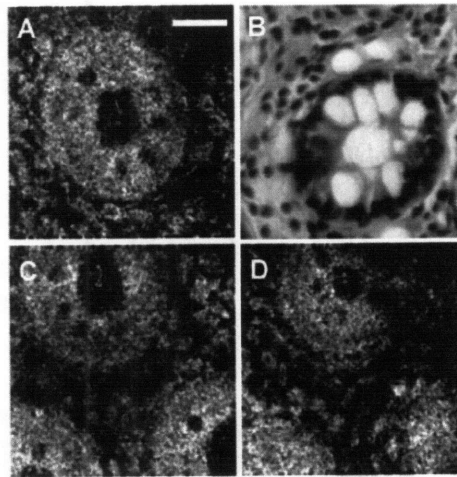


**Figure 12.** Cellular images of a human colonic mucosa *ex vivo*. (A) OCM image of a single crypt structure at  $\sim 100 \mu\text{m}$  below the surface. (B) Representative histology stained with H&E. (C) and (D) are OCM images of a different region at  $\sim 100 \mu\text{m}$  and  $\sim 150 \mu\text{m}$  below the surface, respectively. Features like round crypts, goblet cells, epithelium lining the lumen, lymphoid cells in the lamina propria, and lumen shrinkage over depth can be resolved. Scale bar:  $50 \mu\text{m}$ . Figure is modified slightly from [40].

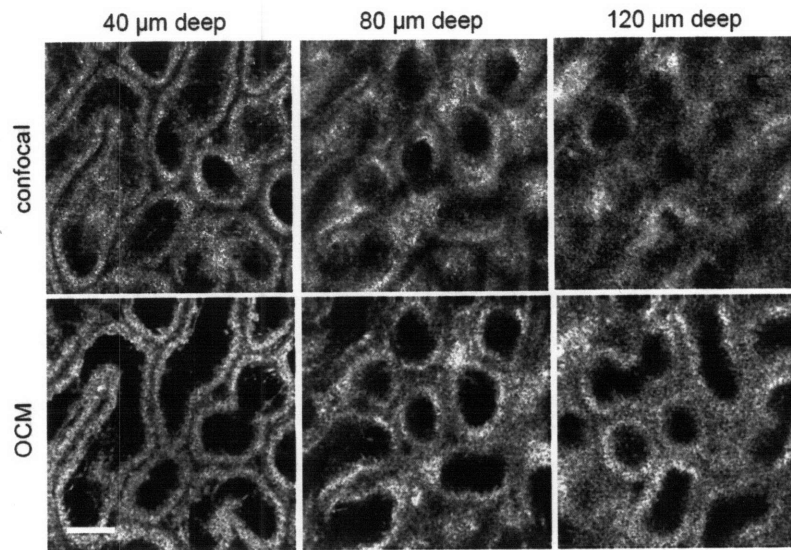


**Figure 13.** A series of confocal (top) as well as OCM (bottom) images in fixed rat kidney. Images are acquired when the focus is at  $\sim 40\ \mu\text{m}$ ,  $\sim 80\ \mu\text{m}$ , and  $\sim 120\ \mu\text{m}$  below the surface (from left to right). The addition of the coherence gating helps reject the unwanted, out of focus scattered light and hence the image contrast in OCM images is higher and cellular details can be delineated more clearly. Scale bar:  $50\ \mu\text{m}$

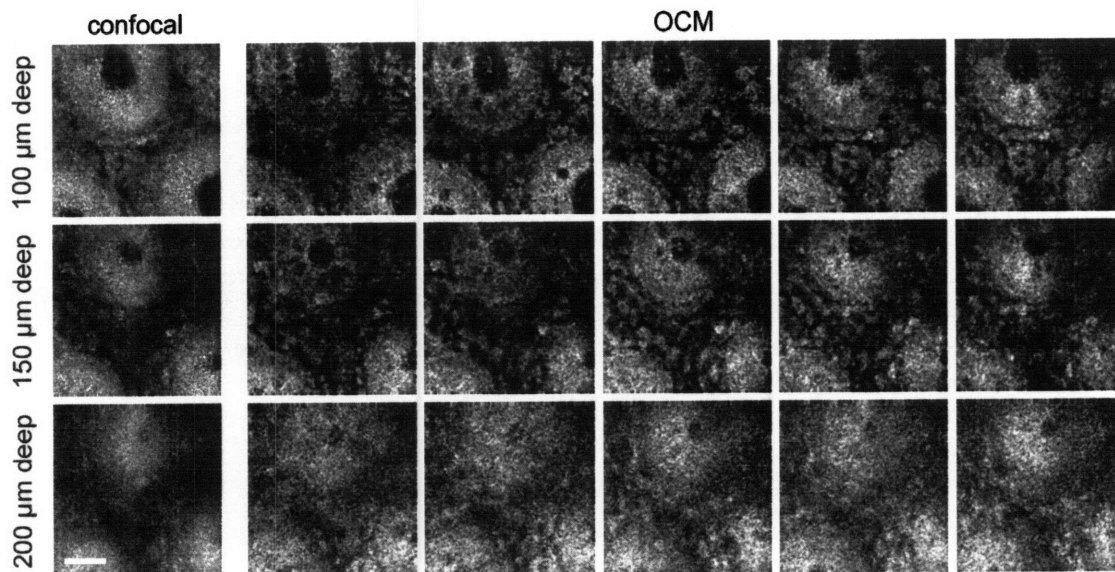


**Figure 14.** A series of confocal as well as OCM images in human colon *ex vivo* when the focus is at  $\sim 100\ \mu\text{m}$ ,  $\sim 150\ \mu\text{m}$ , and  $\sim 200\ \mu\text{m}$  below the surface (from top to bottom). At each focal depth, a series of OCM images with different path length differences ( $4\ \mu\text{m}$  step) from the focus are shown. The quality of confocal gated images degrades much faster than coherence gated images as a function of focal depth, which is a consequence of coherence gate's better resistance to aberration and multiple scattering. Scale bar:  $50\ \mu\text{m}$ .

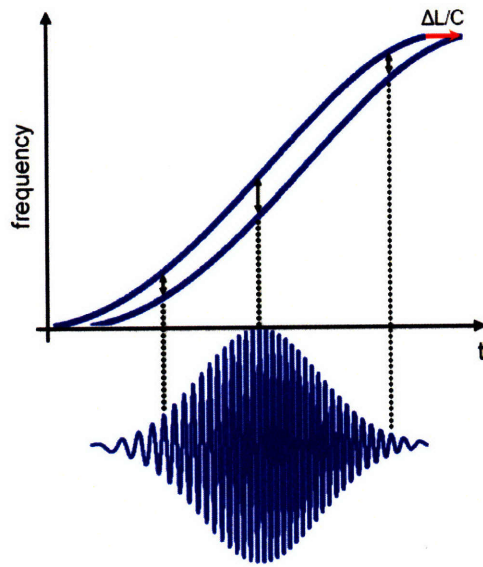


**Figure 15.** Typical nonlinear sweep of a FDML laser and the corresponding interferometric signal with a single reflector on the sample arm and the path difference is set to be  $\Delta L$ . Due to the nonlinear sweep, the beat frequency changes as a function of time and hence it no longer has one-to-one correspondence with the path difference.

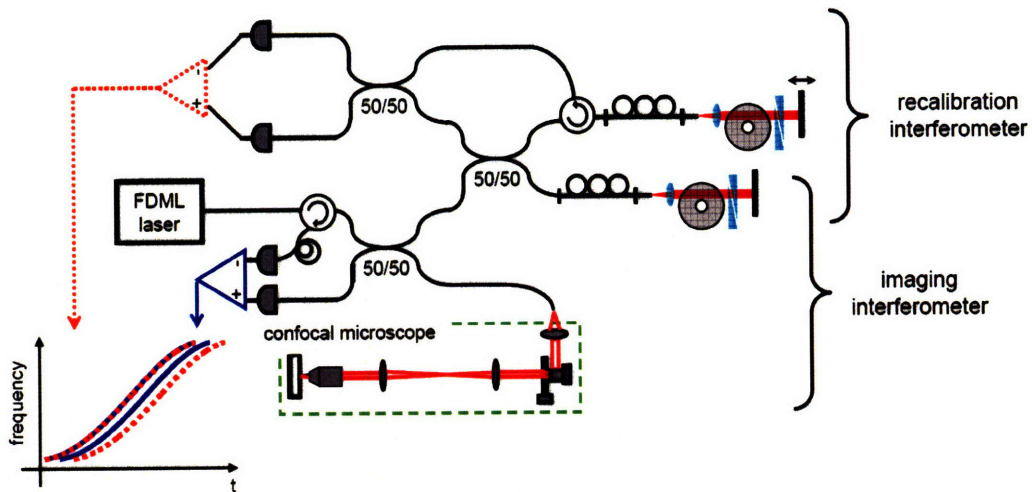


**Figure 16.** Possible schematic of a dual interferometer setup with a common reference arm. The two detector outputs can then be mixed and low-pass filtered to extract the *en face* image from the plane whose path length matches that of the recalibration interferometer's sample arm. Scanning the sample arm of the recalibration interferometer is equivalent to extracting *en face* images from different depths.

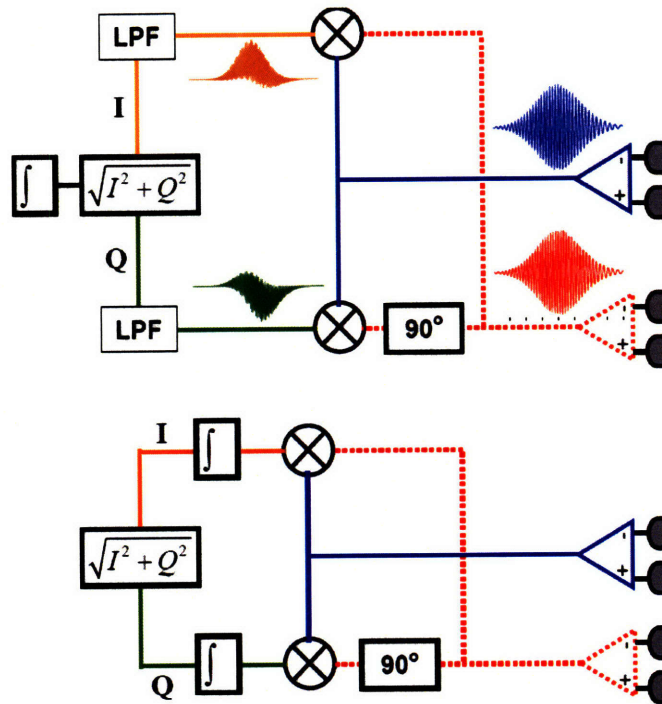


**Figure 17.** Schematics of two possible demodulation electronics. (A) starts with a typical IQ demodulator which is commonly used in communication to extract the envelope signal from a carrier amplitude modulated wave. An integrator then follows to get the amplitude of the envelope signal. (B) is a simplified demodulation electronics. The low-pass filter is replaced directly by an integrator.

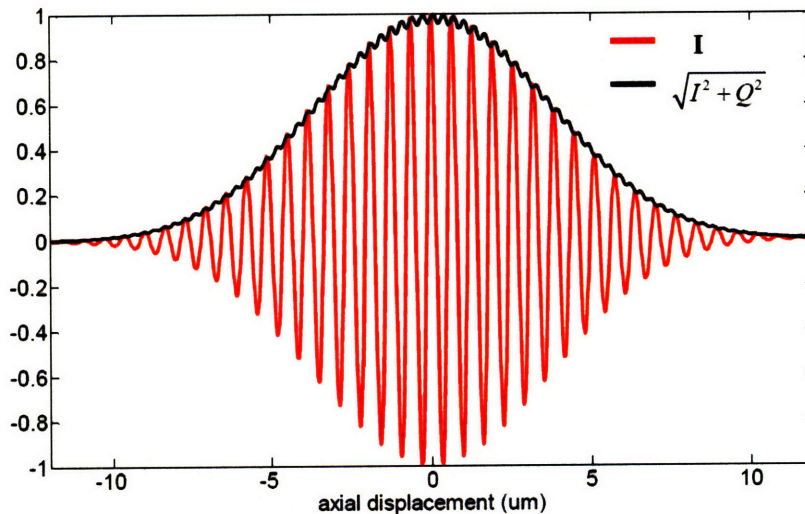


**Figure 18.** The point spread function simulated by using a mirror as the sample and moving it along the axial axis. The addition of an IQ demodulator removes most of the phase dependence except some superimposed zigzag patterns.

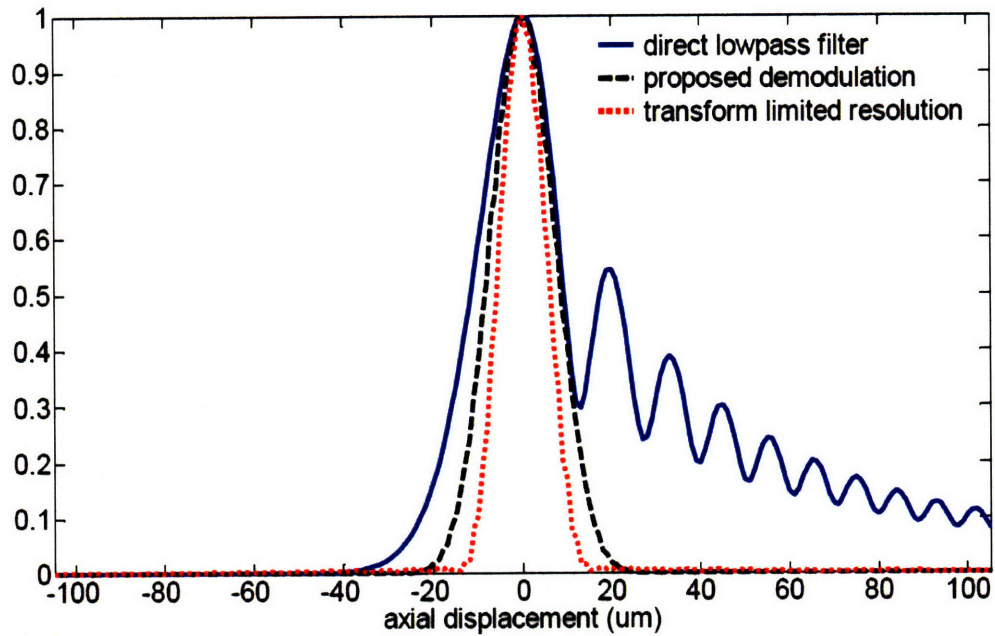


**Figure 19.** Point spread functions simulated with direct band-pass filtering (blue curve) and the proposed scheme (red curve). The proposed scheme improves the *en face* extraction ability compared with that of direct band-pass filtering. Although the achievable axial resolution is ~40% wider than the transform limited resolution, it should be good enough for the purpose of real-time display.

## References

- [1] J. A. Izatt, M. R. Hee, G. M. Owen, E. A. Swanson, and J. G. Fujimoto, "Optical coherence microscopy in scattering media," *Optics Letters*, vol. 19, pp. 590-592, Apr 1994.
- [2] A. L. Clark, A. Gillenwater, R. Alizadeh-Naderi, A. K. El-Naggar, and R. Richards-Kortum, "Detection and diagnosis of oral neoplasia with an optical coherence microscope," *J Biomed Opt*, vol. 9, pp. 1271-1280, Nov-Dec 2004.
- [3] M. Gu, C. Sheppard, and X. Gan, "Image formation in a fiber-optical confocal scanning microscope," *J Opt Soc Am A*, vol. 8, pp. 1755-1761, November 1991.
- [4] M. A. Choma, M. V. Sarunic, C. H. Yang, and J. A. Izatt, "Sensitivity advantage of swept source and Fourier domain optical coherence tomography," *Optics Express*, vol. 11, pp. 2183-2189, Sep 2003.
- [5] J. F. de Boer, B. Cense, B. H. Park, M. C. Pierce, G. J. Tearney, and B. E. Bouma, "Improved signal-to-noise ratio in spectral-domain compared with time-domain optical coherence tomography," *Optics Letters*, vol. 28, pp. 2067-2069, Nov 2003.
- [6] R. Leitgeb, C. K. Hitzenberger, and A. F. Fercher, "Performance of Fourier domain vs. time domain optical coherence tomography," *Optics Express*, vol. 11, pp. 889-894, Apr 2003.
- [7] A. F. Fercher, C. K. Hitzenberger, G. Kamp, and S. Y. Elzaiat, "Measurement of Intraocular Distances by Backscattering Spectral Interferometry," *Optics Communications*, vol. 117, pp. 43-48, May 1995.
- [8] M. Wojtkowski, R. Leitgeb, A. Kowalczyk, T. Bajraszewski, and A. F. Fercher, "In vivo human retinal imaging by Fourier domain optical coherence tomography," *J Biomed Opt*, vol. 7, pp. 457-463, Jul 2002.
- [9] B. Cense, N. Nassif, T. C. Chen, M. C. Pierce, S. Yun, B. H. Park, B. Bouma, G. Tearney, and J. F. de Boer, "Ultrahigh-resolution high-speed retinal imaging using spectral-domain optical coherence tomography," *Optics Express*, vol. 12, pp. 2435-2447, 2004.
- [10] N. A. Nassif, B. Cense, B. H. Park, M. C. Pierce, S. H. Yun, B. E. Bouma, G. J. Tearney, T. C. Chen, and J. F. de Boer, "In vivo high-resolution video-rate spectral-domain optical coherence tomography of the human retina and optic nerve," *Optics Express*, vol. 12, Feb 2004.
- [11] N. Nassif, B. Cense, B. H. Park, S. H. Yun, T. C. Chen, B. E. Bouma, G. J. Tearney, and J. F. de Boer, "In vivo human retinal imaging by ultrahigh-speed spectral domain optical coherence tomography," *Opt Lett*, vol. 29, pp. 480-482, Mar 2004.
- [12] M. Wojtkowski, T. Bajraszewski, I. Gorczynska, P. Targowski, A. Kowalczyk, W. Wasilewski, and C. Radzewicz, "Ophthalmic imaging by spectral optical coherence tomography," *Am J Ophthalmol*, vol. 138, pp. 412-419, Sep 2004.

- [13] M. Wojtkowski, V. J. Srinivasan, T. H. Ko, J. G. Fujimoto, A. Kowalczyk, and J. S. Duker, "Ultrahigh-resolution, high-speed, Fourier domain optical coherence tomography and methods for dispersion compensation," *Optics Express*, vol. 12, pp. 2404-2422, May 2004.
- [14] M. Wojtkowski, V. Srinivasan, J. G. Fujimoto, T. Ko, J. S. Schuman, A. Kowalczyk, and J. S. Duker, "Three-dimensional retinal imaging with high-speed ultrahigh-resolution optical coherence tomography," *Ophthalmology*, vol. 112, pp. 1734-1746, Oct 2005.
- [15] U. Schmidt-Erfurth, R. A. Leitgeb, S. Michels, B. Povazay, S. Sacu, B. Hermann, C. Ahlers, H. Sattmann, C. Scholda, A. F. Fercher, and W. Drexler, "Three-dimensional ultrahigh-resolution optical coherence tomography of macular diseases," *Investigative Ophthalmology & Visual Science*, vol. 46, pp. 3393-3402, Sep 2005.
- [16] V. J. Srinivasan, M. Wojtkowski, A. J. Witkin, J. S. Duker, T. H. Ko, M. Carvalho, J. S. Schuman, A. Kowalczyk, and J. G. Fujimoto, "High-definition and 3-dimensional imaging of macular pathologies with high-speed ultrahigh-resolution optical coherence tomography," *Ophthalmology*, vol. 113, pp. 2054-2065, Nov 2006.
- [17] B. Golubovic, B. E. Bouma, G. J. Tearney, and J. G. Fujimoto, "Optical frequency-domain reflectometry using rapid wavelength tuning of a Cr<sup>4+</sup>:forsterite laser," *Optics Letters*, vol. 22, pp. 1704-1706, Nov 1997.
- [18] S. R. Chinn, E. A. Swanson, and J. G. Fujimoto, "Optical coherence tomography using a frequency-tunable optical source," *Optics Letters*, vol. 22, pp. 340-342, Mar 1997.
- [19] S. H. Yun, C. Boudoux, G. J. Tearney, and B. E. Bouma, "High-speed wavelength-swept semiconductor laser with a polygon-scanner-based wavelength filter," *Optics Letters*, vol. 28, pp. 1981-1983, Oct 2003.
- [20] S. H. Yun, G. J. Tearney, J. F. de Boer, N. Iftimia, and B. E. Bouma, "High-speed optical frequency-domain imaging," *Optics Express*, vol. 11, pp. 2953-2963, Nov 2003.
- [21] M. A. Choma, K. Hsu, and J. A. Izatt, "Swept source optical coherence tomography using an all-fiber 1300-nm ring laser source," *J Biomed Opt*, vol. 10, p. no. 044009 Jul-Aug 2005.
- [22] W. Y. Oh, S. H. Yun, G. J. Tearney, and B. E. Bouma, "115 kHz tuning repetition rate ultrahigh-speed wavelength-swept semiconductor laser," *Optics Letters*, vol. 30, pp. 3159-3161, Dec 2005.
- [23] R. Huber, M. Wojtkowski, and J. G. Fujimoto, "Fourier Domain Mode Locking (FDML): A new laser operating regime and applications for optical coherence tomography," *Optics Express*, vol. 14, pp. 3225-3237, Apr 2006.
- [24] R. Huber, D. C. Adler, and J. G. Fujimoto, "Buffered Fourier domain mode locking: unidirectional swept laser sources for optical coherence tomography imaging at 370,000 lines/s," *Optics Letters*, vol. 31, pp. 2975-2977, Oct 2006.
- [25] M. E. Brezinski, G. J. Tearney, B. E. Bouma, J. A. Izatt, M. R. Hee, E. A. Swanson, J. F.

- Southern, and J. G. Fujimoto, "Optical coherence tomography for optical biopsy. Properties and demonstration of vascular pathology," *Circulation*, vol. 93, pp. 1206-1213, Mar 1996.
- [26] R. Huber, M. Wojtkowski, K. Taira, J. G. Fujimoto, and K. Hsu, "Amplified, frequency swept lasers for frequency domain reflectometry and OCT imaging: design and scaling principles," *Optics Express*, vol. 13, pp. 3513-3528, May 2005.
- [27] J. A. Izatt, M. R. Hee, G. M. Owen, E. A. Swanson, and J. G. Fujimoto, "Optical Coherence Microscopy in Scattering Media," *Optics Letters*, vol. 19, pp. 590-592, Apr 1994.
- [28] J. M. Schmitt, M. J. Yadlowsky, and R. F. Bonner, "Subsurface Imaging of Living Skin with Optical Coherence Microscopy," *Dermatology*, vol. 191, pp. 93-98, 1995.
- [29] A. D. Aguirre, P. Hsiung, T. H. Ko, I. Hartl, and J. G. Fujimoto, "High-resolution optical coherence microscopy for high-speed, in vivo cellular imaging," *Optics Letters*, vol. 28, pp. 2064-2066, Nov 2003.
- [30] A. L. Clark, A. Gillenwater, R. Alizadeh-Naderi, A. K. El-Naggar, and R. Richards-Kortum, "Detection and diagnosis of oral neoplasia with an optical coherence microscope," *Journal of Biomedical Optics*, vol. 9, pp. 1271-1280, Nov-Dec 2004.
- [31] Y. H. Zhao, Z. P. Chen, C. Saxer, S. H. Xiang, J. F. de Boer, and J. S. Nelson, "Phase-resolved optical coherence tomography and optical Doppler tomography for imaging blood flow in human skin with fast scanning speed and high velocity sensitivity," *Optics Letters*, vol. 25, pp. 114-116, Jan 2000.
- [32] V. Westphal, S. Yazdanfar, A. M. Rollins, and J. A. Izatt, "Real-time, high velocity-resolution color Doppler optical coherence tomography," *Optics Letters*, vol. 27, pp. 34-36, Jan 2002.
- [33] T. Q. Xie, Z. G. Wang, and Y. T. Pan, "High-speed optical coherence tomography using fiberoptic acousto-optic phase modulation," *Optics Express*, vol. 11, pp. 3210-3219, Dec 2003.
- [34] M. Pircher, E. Goetzinger, R. Leitgeb, and C. K. Hitzenberger, "Transversal phase resolved polarization sensitive optical coherence tomography," *Physics in Medicine and Biology*, vol. 49, pp. 1257-1263, Apr 2004.
- [35] M. A. Choma, A. K. Ellerbee, C. H. Yang, T. L. Creazzo, and J. A. Izatt, "Spectral-domain phase microscopy," *Optics Letters*, vol. 30, pp. 1162-1164, May 2005.
- [36] C. Joo, T. Akkin, B. Cense, B. H. Park, and J. E. de Boer, "Spectral-domain optical coherence phase microscopy for quantitative phase-contrast imaging," *Optics Letters*, vol. 30, pp. 2131-2133, Aug 2005.
- [37] C. Y. Xu, C. Vinegoni, T. S. Ralston, W. Luo, W. Tan, and S. A. Boppart, "Spectroscopic spectral-domain optical coherence microscopy," *Optics Letters*, vol. 31, pp. 1079-1081, Apr 2006.

- [38] M. Rajadhyaksha, R. R. Anderson, and R. H. Webb, "Video-rate confocal scanning laser microscope for imaging human tissues in vivo," *Applied Optics*, vol. 38, pp. 2105-2115, Apr 1999.
- [39] D. C. Adler, R. A. Huber, and J. G. Fujimoto, " Phase-sensitive OCT using buffered FDML lasers at up to 370,000 scans per second," *Photonics West/BiOS*, presentation 6429-56, Jan 2007
- [40] S. W. Huang, A. D. Aguirre, R. A. Huber, D. C. Adler, and J. G. Fujimoto, "Swept source optical coherence microscopy using a Fourier domain mode-locked laser," *Optics Express*, vol. 15, pp. 6210-6217, May 2007



## **CHAPTER 3 – Line Scan Optical Coherence Microscopy**

### **3.1 Linnik type Optical Coherence Microscopy**

Line scan OCM described in this chapter is fundamentally different from time-domain OCM and swept source OCM in the sense that it is based on the Linnik interference microscope. Figure 1 shows a schematic of a typical Linnik interference microscope. Using two identical objectives in both reference and sample arms, a Linnik interference microscope achieves an optical sectioning effect similar to that in confocal microscopy, with slightly better light collection. Instead of a physical pinhole, a synthetic pinhole is formed due to the fact that appreciable interference signal can be generated only when the phase front of the reflected light probing the sample matches that from the reference arm, termed as correlation gate [1]. The correlation gate scales with respect to NA the same way as the confocal gate does and hence it has been proposed to add the coherence gate to the Linnik interference microscope so that low NA optics can be used and its robustness to aberration and multiple scattering is improved [2, 3]. The microscope system is generally referred to as full-field OCM and has the advantages of easy dispersion compensation, low cost, and reduced speckle. Nevertheless, it has a major drawback of low sensitivity because neither correlation gate nor coherence gate can remove the out-of-focus light before detection.

### **3.2 Line Scan Optical Coherence Microscopy**

Due to its simplicity and low-cost, full-field OCT/OCM has been widely investigated in recent years [2, 3, 5, 6]. However, full-field illumination and detection has limited sensitivity because of the significant amount of incoherence scattered light. Line illumination and detection reduces incoherent scattered light and pixel cross-talk compared with full-field illumination. Higher sensitivity is expected and hence line scan OCM has the potential to achieve cellular imaging in highly scattering tissues. In this chapter, we demonstrate the feasibility of cellular imaging in highly scattering tissues using line scan OCM.

#### **3.2.1. Motivations**

Modification of the full-field OCM to accommodate line illumination and detection has several advantages. First, line illumination reduces pixel cross-talk and a weak confocal gate (FWHM  $\sim 80 \mu\text{m}$ ) helps reject out-of-focus light. Together the sensitivity can be increased by more than an order of magnitude. Second, the correlation gate is widened so that gate coordination is not so critical as it is for full-field OCM [4]. Finally, line detection is less sensitive to sample motion compared with full-field detection because phase sensitive information is acquired more rapidly, before significant phase averaging effects can occur.

Unlike confocal type OCM, which has been implemented by raster scanning a tightly focused beam across the sample [7-9], line scan OCM only requires a single-axis scanning. Although there has been considerable interest in developing miniaturized fast scanning devices for two-dimensional scanning in endoscopic microscopy applications [10-14], it remains challenging to perform precise two-dimensional scanning with small device sizes. Line scan OCM circumvents the problem not only because a miniaturized high speed single-axis scanner is readily available, but also due to the fact that complex multiple-lens telecentric relay system is not required to optimize the optical performance.

### **3.2.2. System setup and characterization**

Figure 2 shows the schematic of the experimental setup. The line scan OCM system was based on a Linnik type interference microscope with two identical microscope objectives (Zeiss, 10x Achromat, Infinity corrected, NA=0.3, WD=3.1 mm, Water immersion) in the sample and reference arms. A compact, commercially-available broadband Ti:Sapphire laser (FemtoLasers, Femtosource compactOCT) was used to generate a spectral bandwidth of 80 nm at a center wavelength of 820 nm. 50 mW average power was coupled into a single mode fiber and delivered to the interferometer which gave 25 mW incident on the sample. A bulk glass (SF57, 5 cm) is used for stretching the pulse to a few ps so that spectral modulation due to nonlinear effect in the fiber can be minimized.

Line illumination was achieved by the combination of a spherical focusing lens and a plano-concave cylindrical lens. The design has the advantage that it does not require focusing with a cylindrical singlet lens and hence the aberration is less severe. Nevertheless, the aberration is severe enough to increase the focused line width on the sample ( $\sim 5 \mu\text{m}$ ) by about a factor of 3 from the theoretical value. The reference arm power was controlled by a neutral density filter,

and a glass blank was used in the sample arm to balance the dispersion. Light from the sample and reference arms were recombined by the beam splitter and imaged onto a high speed, 1024 pixel line scan CCD camera (Atmel AViiVA M2 CL) with 12 bit A/D range. The interference signal was modulated by actuating the reference mirror with a piezoelectric transducer (PI, PL055.30,  $2.2\mu\text{m}@100\text{V}$ , Resonant frequency  $>300\text{ kHz}$ , Blocking force  $>500\text{ N}$ ), using four integrating-bucket technique with sinusoidal phase modulation to extract the interference component [3]. Modulation amplitude and synchronization phase between the modulation and the image acquisition is adjusted experimentally with a mirror as the sample [15]. The 3-step procedure is: 1. the synchronization phase is adjusted to minimize the image intensity; 2. add  $56^\circ$  to the synchronization phase; 3. the modulation amplitude is adjusted to minimize the spatial fringe contrast. *En face* images were generated by transversely scanning the sample orthogonal to the illumination line with a precision translation stage. A series of *en face* images at different depths were also acquired by translating the sample in the axial direction.

The line scan camera was read at  $\sim 52\text{ Mpixel/s}$ , corresponding to an  $f = 51.6\text{ kHz}$  line acquisition rate, while the PZT was sinusoidally actuated at  $f/4 = 12.9\text{ kHz}$  and synchronized to the camera frame grabber. Typically, 30 line scans from each of the four-quadrant integrating-bucket (120 total line scans) were averaged to increase the signal-to-noise ratio, and resulted in a line acquisition speed of 430 lines/second. Each *en face* image consisted of 256 lines and was acquired in 0.6 second. The magnification and the scanning speed of the system were chosen such that the image size is  $256 \times 256$  pixels over the field-of-view of  $256\ \mu\text{m} \times 256\ \mu\text{m}$ . The axial point spread function of the system was measured by translating a mirror in the sample arm. Figure 3(a) shows the measured axial resolution of  $\sim 3\ \mu\text{m}$  in water. Figure 3(b) shows the coherence gated *en face* OCM image of a USAF target in the sample arm. The smallest group 7, element 6 bars were resolved, indicating a  $\sim 2\ \mu\text{m}$  transverse resolution.

The detection sensitivity of the system can be expressed as:  $S = 2R_{\text{ref}}/N\zeta = 4R_{\text{inc}}/N\zeta$  [3], where  $R_{\text{ref}}$  is the reflectivity of the reference arm power,  $R_{\text{inc}}$  is the proportion of the incoherent light backscattered by structures within the sample but located outside the coherence volume,  $N$  is the number of images averaged, and  $\zeta$  is the full-well capacity of the CCD pixels. For optimal operation,  $R_{\text{ref}} = 2R_{\text{inc}}$  [3]. Therefore the incoherent scattered light limits the maximum power applied to the system before the CCD camera saturates and hence limits the detection sensitivity. For full-field illumination and detection, the typical amount of incoherent scattered light in

biological tissues is  $\sim 1\%$  ( $R_{\text{inc}} = 1\%$ ) [3]. Line illumination dramatically reduces the amount of incoherent scattered light compared to full-field illumination due to the reduced illumination volume outside the coherence volume. Using line illumination,  $R_{\text{inc}}$  was measured to be  $< 0.1\%$  in the highly scattering medium, more than 10 times smaller than that in full-field OCT. Therefore a 10 dB higher sensitivity could be achieved using line illumination. Figure 4 compares the sensitivity with different numbers of images averaged ( $N$ ) for line illumination versus full-field illumination. The experimental comparison with full-field illumination was performed by removing the cylindrical lens and adjusting the position of the spherical focusing lens. By using the same camera, the effect of full-well capacity variations can be eliminated. The sensitivity was measured by the mirror reflection with calibrated attenuation in the sample arm. For full-field illumination, an OD = 1 neutral density filter (total attenuation OD = 2) was used in the reference arm, which gave 1% of returned power in the reference arm ( $R_{\text{ref}} = 1\%$ ), and the system sensitivity with 30 averages was measured to be 83 dB, consistent with previously published full-field OCT results [3, 6]. For line illumination, the incoherent scattered light in the highly scattering media is more than 10 times less than full-field illumination. This suggests it is possible to apply more power in the reference arm (or equivalently to apply more power in the sample arm before the camera saturates, due to the lower amount of incoherent scattered light). In the experiment, we used an OD = 1.5 neutral density filter (total attenuation OD = 3) in the reference arm, which gave  $R_{\text{ref}} = 0.1\%$ . With 30 averages, 93 dB detection sensitivity can be achieved, demonstrating a  $\sim 10$  dB higher sensitivity compared with full-field illumination case. The detection sensitivity also increases as more averages are performed until the effect of mechanical and thermal instabilities shows up and saturates the sensitivity.

### 3.2.3. Imaging results

Figure 5 shows images and H&E stained histology of a fixed rat kidney. Figure 5(a) and 5(b) were acquired when the focus is at  $\sim 40 \mu\text{m}$  and  $\sim 120 \mu\text{m}$  below the surface, respectively. The cell lining along the kidney tubules is readily visible and small regions of bright reflectivity, consistent with nuclei, can also be observed in the images. Figure 6 shows images of pig intestine *ex vivo*. Specimens were preserved in the phosphate-buffered saline (PBS) and imaged within a few hours after excision. During the imaging, PBS was used with the immersion microscope objective to maintain tissue hydration and facilitate index matching. Figure 6(a) and

6(b) were taken near the surface (50  $\mu\text{m}$  and 100  $\mu\text{m}$ , respectively) and villi structure characteristic of small intestine is clearly depicted. Epithelial cells can also be identified in the images. Figure 6(c) and 6(d) were taken at deeper depths (200  $\mu\text{m}$  and 250  $\mu\text{m}$ , respectively) and crypt structures begin to show up. Cells lining the crypt can also be observed.

Figure 7 shows representative images of a human colon specimen *ex vivo*. An *en face* image at 100  $\mu\text{m}$  below the surface is shown in Figure 7(a). Detailed structures such as the crypt lumens, the epithelial layer, and lamina propria were clearly visualized. Individual goblet cells containing translucent mucin could be seen within the epithelial layer. The image demonstrates the high-resolution, cellular level imaging capability of the line scan OCM. After imaging, specimens were fixed in formalin and processed for histology. In addition to the standard cross-sectional plane, sectioning was performed in the *en face* plane to facilitate comparison to the OCM image plane. Histology is representative because exact registration of the histological section to the area of OCM imaging and especially the depth of the section are difficult. Representative *en face* histology stained with H&E is shown in Figure 7(c).

Three-dimensional imaging was performed by acquiring a stack of *en face* images when translating the sample in depth. A total of 80 *en face* images with 5  $\mu\text{m}$  depth interval were acquired in 48 seconds with a frame rate  $\sim 2$  Hz. With intensity threshold segmentation, lower scattering structures including crypt lumen (CL) and mucin-containing goblet cells were segmented. A three-dimensional view of a single crypt lumen is shown in Figure 7(b). The crypt lumen (CL) was visualized to almost its full depth, with individual goblet cells surrounding the crypt lumen. The lumen diameter decreases as the sectioning depth increases into the mucosa. A representative cross-sectional histology is shown in Figure 7(d).

#### **3.2.4. Summary**

This study demonstrates a line-scanning optical coherence microscopy (OCM) system. A spatial resolution of  $\sim 2 \mu\text{m} \times \sim 3 \mu\text{m}$  (transverse  $\times$  axial) was achieved. The sensitivity with 30 averages was measured to be 93 dB, giving an imaging speed of  $\sim 2$  frames per second. The imaging speed could be doubled to  $\sim 4$  Hz by using two integrating-bucket demodulation [16]. Compared with full-field OCM, line scan OCM has the disadvantage of requiring expensive laser or SLD light sources versus low-cost thermal light sources. However, line illumination reduces the amount of incoherent scattered light and pixel cross-talk in scattering tissues and therefore

achieves higher detection sensitivity compared with full-field illumination. The use of line scan cameras also promises to enable *in vivo* imaging by reducing sensitivity to sample motion compared with full-field camera detection because phase sensitive information is acquired rapidly before significant phase averaging effects can occur. Line scan endoscopic OCM would require techniques for line illumination and detection, but compared with standard point scanning OCM, it has the advantage of requiring only one dimensional scanning.

### **3.3 Future Work**

#### **3.3.1. Camera**

Dubois *et al.* has shown that the system sensitivity is proportional to the camera's full-well capacity (FWC) [3]. The camera we used for this study has only 180 ke FWC, typical of silicon camera, and averaging of 30 frames is necessary to achieve 93 dB sensitivity. An InGaAs camera, in general, has FWC an order of magnitude higher than silicon camera and Oh *et al.* has shown that full-field OCM using InGaAs camera has superior performance [6]. Use of InGaAs camera also enables the operation at longer wavelength to reduce scattering. Goodrich's new model, SUI SU-LDH-1.7RT/LC, offers FWC of 125 Me and readout noise less than 25 ke. Sensitivity of >95 dB can be supported by the camera without the need for averaging.

#### **3.3.2. Achromatic Cylindrical Lens Design**

As mentioned in the section 3.2.2, aberration of the cylindrical lens increases the focused line width on the sample by about a factor of 3. It not only reduces the system sensitivity by increasing the incoherent light, but also lowers the light collection efficiency. Design of diffraction limited cylindrical lenses can help improve the system performance. Figure 8 shows the design of the focusing cylindrical lens. In combination with the current 10x objective, a 1.7  $\mu\text{m}$  and 700  $\mu\text{m}$  line focus is anticipated and confirmed by the Zemax simulation.

A lens system that provides different magnification in x (scanning, orthogonal to the line focus) and y (parallel to the line focus) axes is preferable but not feasible in this study because it requires combination of diffraction limited cylindrical lenses. Of note, Nyquist sampling criterion is satisfied differently in the two axes. For x axis, scanning speed is the key parameter that is used to meet the criterion. The magnification, on the other hand, is set to optimize the

light collection efficiency and the confocal gating power. The situation is different for y axis because the magnification is the only parameter that can be chosen to meet the criterion. For a typical camera which has square pixel elements, it means that  $\frac{M_y}{M_x} = 2$  is required to optimize the light collection efficiency and satisfy Nyquist sampling criterion at the same time. Nevertheless, the design will suffer from loss of confocal gate. As a compromise, a lens system which provides a magnification ratio of  $\sim 1.6$  is designed and shown in figure 9.

### 3.3.3. Demodulation Method

The demodulation method we used for this study follows the one proposed by Arnaud Dubois and the performance is well described in Ref [15]. The four integrating-bucket technique with sinusoidal phase modulation has the unique advantage that the modulation frequency can be as high as several tens of kHz and so it permits high speed imaging. Nevertheless, sinusoidal modulation is not desirable when the PZT actuator is used to mechanically modulate the phases. It is well known that PZT exhibits hysteresis (see figure 10) and hence any bi-directional modulation such as sinusoidal modulation will generate phase shift errors and eventually lower the sensitivity. Either the use of a sawtooth modulation or a closed loop system can solve the problem but none of the method works at high frequency.

In this study, each line is modulated and demodulated individually and then all the line images are combined to form an *en face* image. If we want to have an image with 512 lines and an imaging speed of 30 Hz, a PZT modulation frequency of 15 kHz (512x30) is required. Another method is collect lines to form images before demodulation. The method seems trivial, but it does not work with Dubois' algorithm because of its dependence on synchronization phase [15]. Figure 11 shows the simulation result. The colored blocks represent the integration buckets required for demodulation. The synchronization phase changes for different line quadruplets and it is clear that the demodulation is unsuccessful in some regions (red square).

Figure 12 shows a diagram of the proposed modulation method. A triangular waveform (black curve) with amplitude of  $2.5\pi$  is used to modulate the phases. Linear phase modulation has the advantage that synchronization phase plays no role. The modulation frequency is only half of the imaging speed. If we want to have an imaging speed of 30 Hz, the required modulation frequency is only 15 Hz and a closed loop PZT actuator system can be used to

further minimize the phase shift errors. The dashed curve represents the line scanning waveform and the scan rate has to be increased by a factor of five, the number of required buckets. Of note, a line scan OCM with this method is very similar to a full-field OCM with a progressive scan area camera, which captures a frame line by line, except that the confocal gate and the pixel cross-talk reduction are still present.

The proposed method has a major disadvantage that the corresponding line in the next integration bucket is acquired after the acquisition of all lines in the first bucket and therefore the phase correlation between the corresponding lines is not as high as that using the current method. The effect can be considered equivalent to perturbations of the phase shift increment. The choice of Hariharan algorithm (Figure 11) is justified because of its extreme robustness to errors [17].

### **3.4 Preliminary Comparison between Three OCM Imaging Systems**

Table 1 summarizes some important parameters as well as the performance of the three OCM systems running in our laboratory. So far, time domain OCM system provides the best quality imaging results. Nevertheless, it is possible to further improve the two other OCM systems as mentioned in chapter 2 and this chapter. It is worthwhile at this point to compare the two other OCM systems with the time domain OCM and try to evaluate their potentials.

Figure 13 is an OCT image of a hamster cheek pouch *ex vivo*. Specimens were preserved in the Dulbecco's modified Eagle's media and imaged within two hours after excision. Details about the animal handling can be found in the appendix. For the following OCM comparison, images will be taken at the epithelium, lamina propria, and muscularis mucosa. Figure 14-16 shows the representative images taken with three different OCM systems. The colormap of all the following images are black-on-white, meaning that scatterers like the nucleus will appear dark in the images.

Although epithelial cells can be discerned in all systems, the contrast in swept source system is evidently lower. This is understandable since swept source OCM so far provides the worst sectioning ability. Figure 17 shows a better comparison between swept source OCM and time domain OCM. Figure 17(a) is a time domain image and epithelial cells can be clearly delineated. To mimic the worse sectioning ability of swept source OCM, three OCM images at different depths are averaged and the result is shown in figure 17(b). Loss of contrast is evident and there is not much difference from the image taken with swept source OCM, which is shown in figure

17(c). As mentioned in chapter 2, we have recently developed FDML lasers with tuning ranges of  $\sim 160$  nm using specially matched semiconductor optical amplifiers (SOA) and it suggests that axial resolutions can be improved to  $\sim 5$   $\mu\text{m}$ . Further improvement of the tuning range of FDML lasers is possible by combining two or more SOA gain stages inside the laser cavity. This approach is similar to multiplexing techniques used in photonics to increase bandwidths. A coupler is placed in the cavity to divide the light into two parallel paths containing two SOA's with shifted center wavelengths. The amplified outputs are recombined in a second coupler, increasing the total bandwidth by a factor of 2.

Line scan OCM shows images comparable to time domain OCM in superficial layers such as epithelium and lamina propria. However, due to the higher scattering at 800 nm and the lower system sensitivity, the images at deeper layers such as muscularis are worse. As mentioned previously, the system sensitivity can be increased by use of a camera with higher FWC, achromatic cylindrical lenses, and a more robust demodulation scheme. Figure 18 shows a better comparison between line scan OCM and time domain OCM. Interestingly, it is evident that line scan OCM has less speckle. The difference between resolutions is so small that it is unlikely to be the cause. Most likely it is because line scan OCM performs parallel detection and hence the pixel dwell time is longer than time domain OCM. Time averaging leads to the reduction of speckle noise.

It is worthwhile to mention the analogy between Fourier domain detection and line scan detection. It is helpful to refer back to figure 8 in chapter 1. For applications which require fast acquisition of cross-section images, Fourier domain detection has the advantage that it probes different depths in parallel and hence higher imaging speed can be achieved [18-20]. However, for applications which emphasize *en face* images like most OCM, there is no inherent advantage of Fourier domain detection compared with time domain detection [9]. For these applications, line detection plays the role of parallel detection. Since time domain OCM does not have too much trouble with imaging speed, it is unlikely that people will use the parallel detection to further increase the imaging speed. Rather, the longer pixel dwell time can help reduce the speckle noise, which is destructive for coherence microscopy.

## **Acknowledgements**

The contributions of several individuals to this chapter must be mentioned. All the fresh excised human tissues are provided by Dr. James Connolly from the Beth Israel Deaconess Medical Center. Former Post-doctoral associate Yu Chen led the team to develop the system. Former graduate student Aaron Aguirre helped design the system and analyze the data.

## Figures

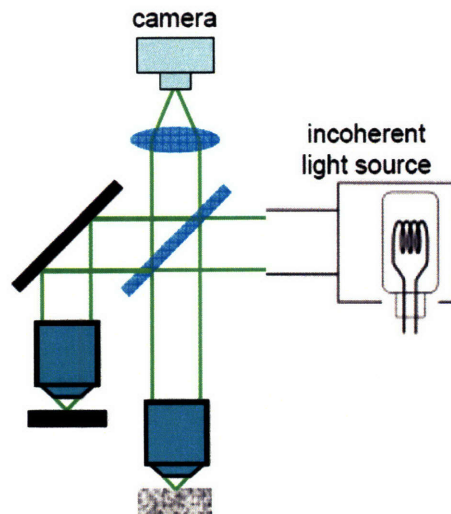


**Figure 1.** Schematic of a typical Linnik interference microscope. Using two identical objectives in both reference and sample arms, a Linnik interference microscope achieves an optical sectioning effect similar to that in confocal microscopy, with slightly better light collection.

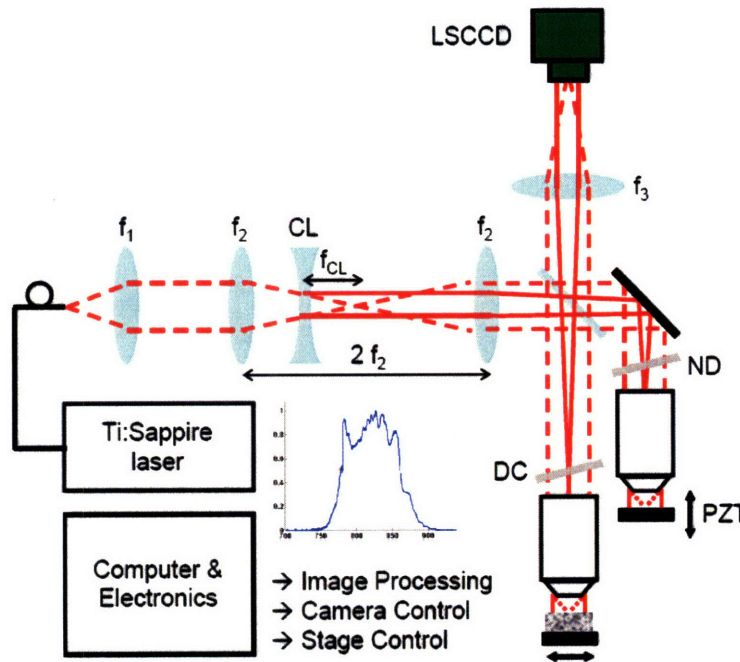


**Figure 2.** Schematic of the line scan OCM system for cellular imaging. CL, cylindrical lens; ND, neutral density filter; DC, glass plate for dispersion compensation; PZT, piezoelectric transducer; LSCCD, line scan CCD camera. A compact, commercially-available broadband Ti:Sapphire laser was used to generate a spectral bandwidth of 80 nm at a center wavelength of 820 nm. The focal length of the lenses are  $f_1 = 50$  mm,  $f_2 = 150$  mm,  $f_{CL} = -80$  mm,  $f_3 = 200$  mm. Figure is modified slightly from [21].

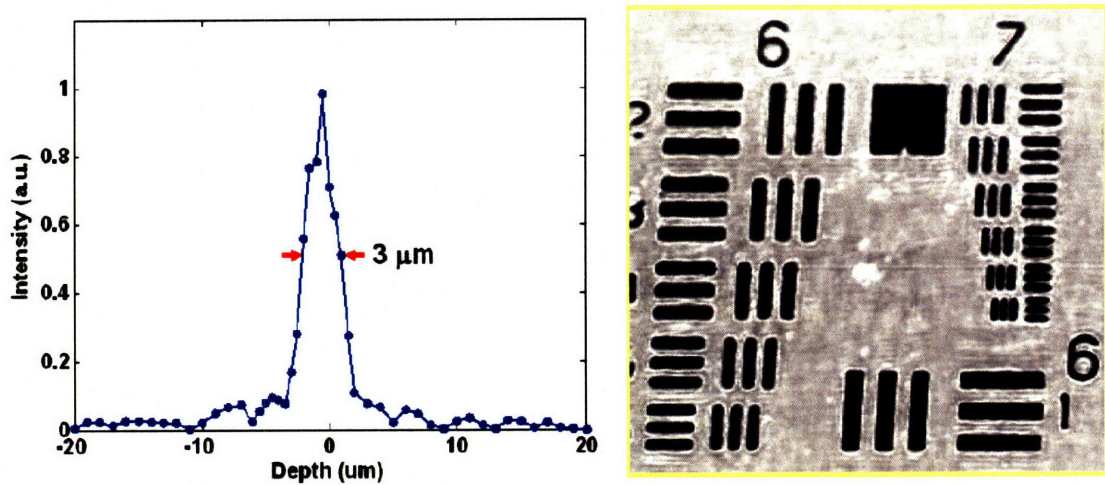


**Figure 3.** Line scan OCM system characterization. (A) Measured axial point spread function with  $\sim 3 \mu\text{m}$  FWHM in water. (B) Image of a USAF resolution target demonstrating a transverse resolution of  $\sim 2 \mu\text{m}$ . Figure is modified slightly from [21].

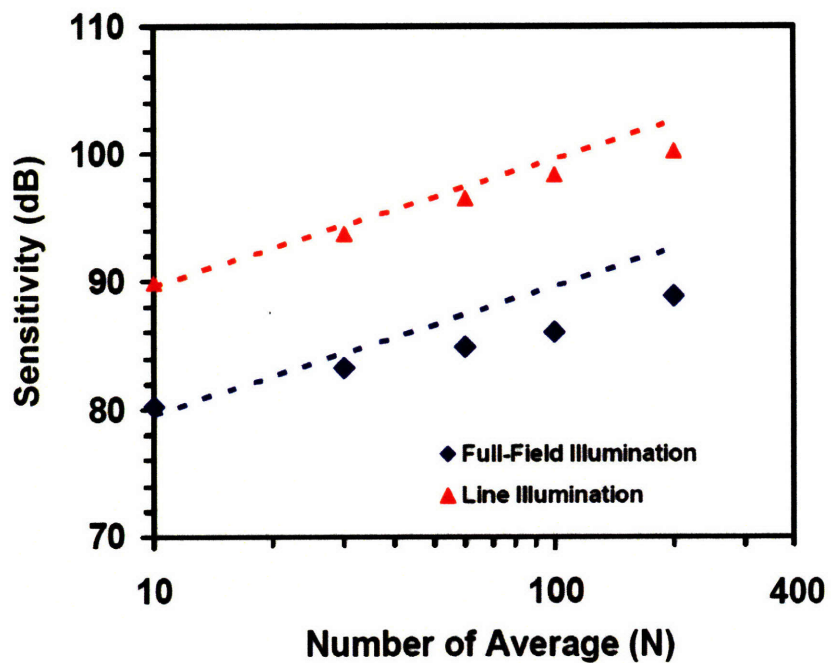


**Figure 4.** Comparison of system sensitivity versus the number of averages (N) using line illumination ( $R_{\text{ref}} = 0.1\%$ ) and full-field illumination ( $R_{\text{ref}} = 1\%$ ). Line illumination (red triangles) achieves  $\sim 10$  dB higher sensitivity than full-field illumination (blue diamonds) for a given averaging number. Dotted lines indicate the theoretical values. Figure is modified slightly from [21].

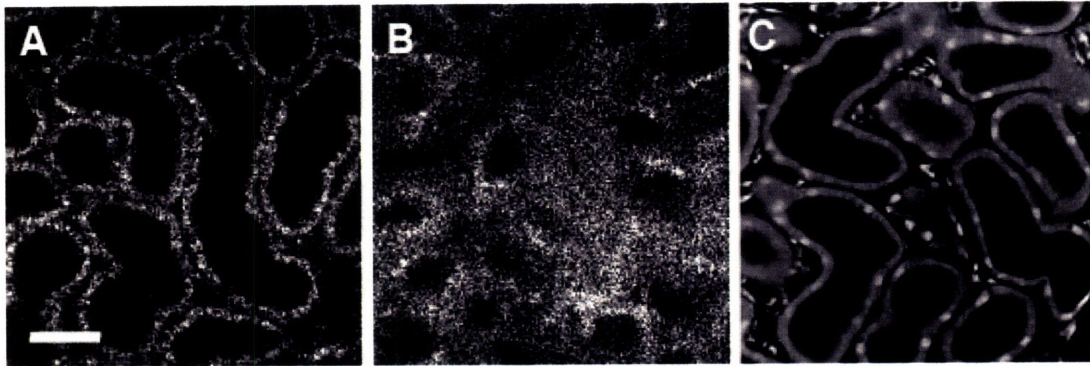


**Figure 5.** Cellular images of a fixed rat kidney. (A) and (B) are OCM images at  $\sim 40 \mu\text{m}$  and  $\sim 120 \mu\text{m}$  below the surface, respectively. (C) Representative histology stained with H&E. The cell lining along the kidney tubules and nuclei can be observed. Scale bar:  $50 \mu\text{m}$ .

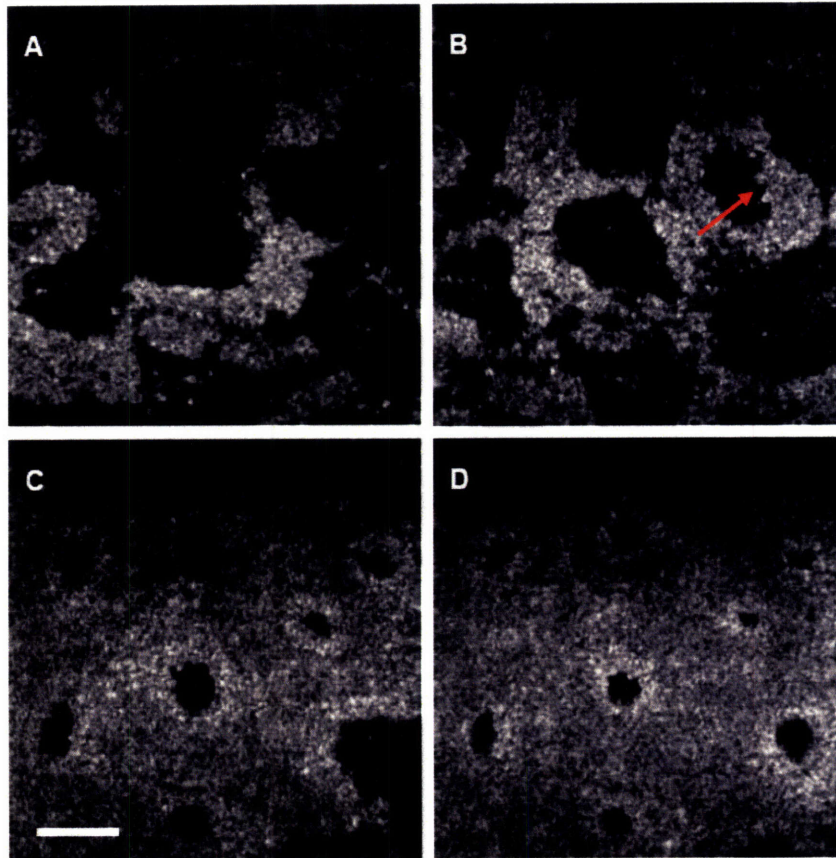


**Figure 6.** Images of pig intestine *ex vivo*. A and B were taken near the surface ( $50 \mu\text{m}$  and  $100 \mu\text{m}$ , respectively) and villi structure characteristic of small intestine is clearly depicted. Epithelial cells can also be identified in the images. C and D were taken at deeper depths ( $200 \mu\text{m}$  and  $250 \mu\text{m}$ , respectively) and crypt structures begin to show up. Cells lining along the crypt can also be observed. Scale bar:  $50 \mu\text{m}$ .

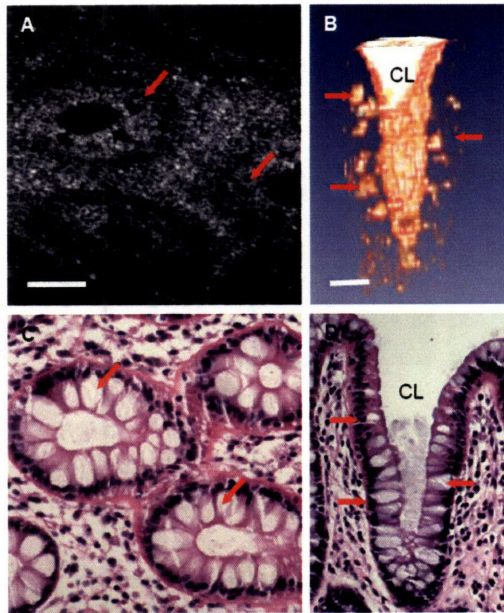


**Figure 7.** Cellular images of human colon specimen *ex vivo*. (A) OCM image of crypt structures at  $\sim 100 \mu\text{m}$  below the surface. (B) 3D rendering with low-scattering crypt lumen (CL) and goblet cells (red arrows) segmented out. (C) Representative *en face* histology of the colon. (D) Corresponding cross-section histology showing crypts lumen (CL) and goblet cells (red arrows). Scale bar:  $50 \mu\text{m}$ . Figure is modified slightly from [21].

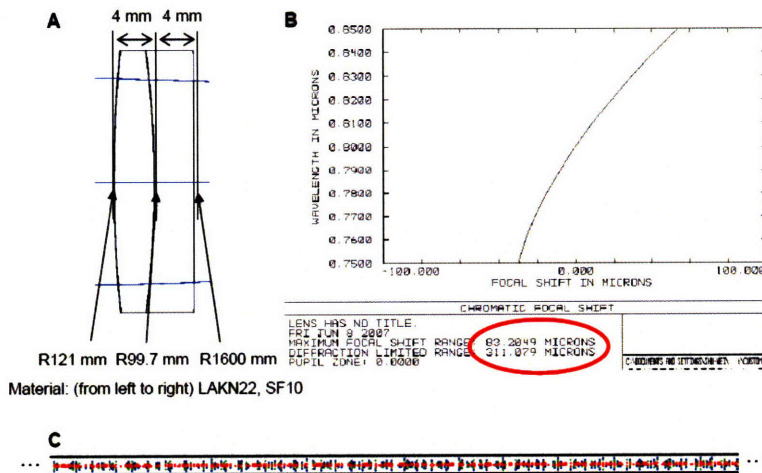


**Figure 8.** Design of the focusing cylindrical lens and the Zemax simulation results. (A) Material, thickness, and surface curvature of the lens which has an  $192.7 \text{ mm}$  back focal length. (B) Analysis of chromatic aberration. The maximum focal shift is only one fourth of the depth-of-focus and good achromatism is demonstrated. (C) Spot diagram at the focus. The black line represents the Airy disk and the fact all the ray tracing points locate within it indicates that the diffraction limited line focus is achievable. Three wavelengths are used in the simulation:  $750 \text{ nm}$  (blue),  $800 \text{ nm}$  (red), and  $850 \text{ nm}$  (green).

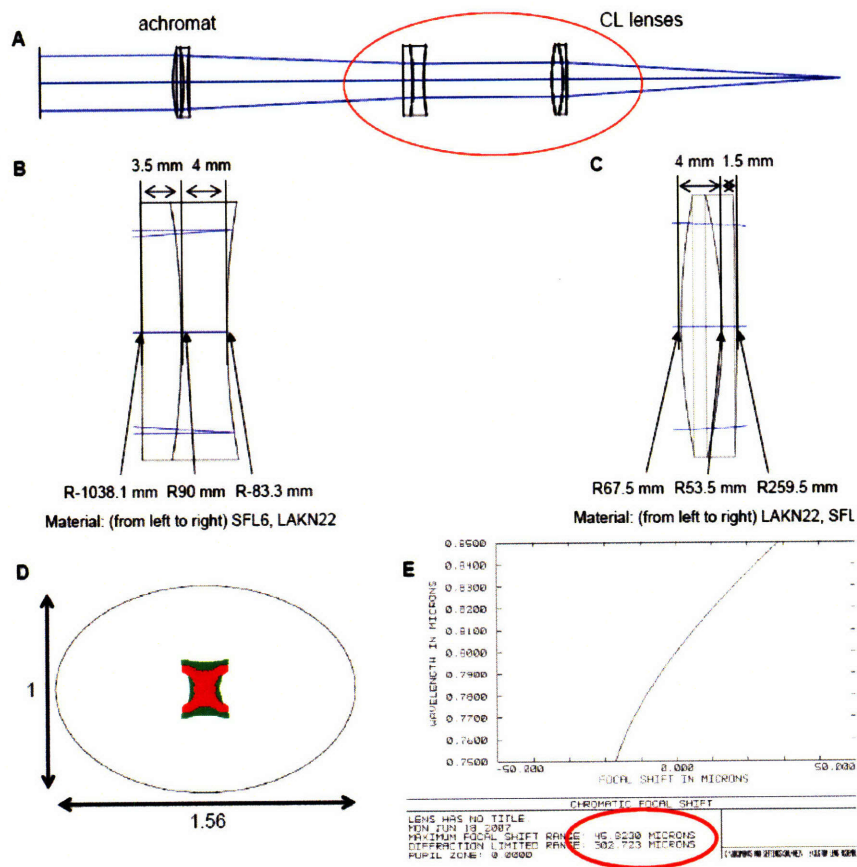


**Figure 9.** Design of the lens system that provides different magnification in x and y axes and the Zemax simulation results. (A) Simulation model. (B) Material, thickness, and surface curvature of the first lens which has a -145 mm back focal length. (C) Material, thickness, and surface curvature of the second lens which has a 98.4 mm back focal length. (D) Spot diagram at the focus. The black line represents the Airy disk and a magnification ratio of 1.56 is demonstrated. The fact all the ray tracing points locate within it indicates that the diffraction limited line focus is achievable. Three wavelengths are used in the simulation: 750 nm (blue), 800 nm (red), and 850 nm (green). (E) Analysis of chromatic aberration. The maximum focal shift is only one seventh of the depth-of-focus and good achromatism is demonstrated.

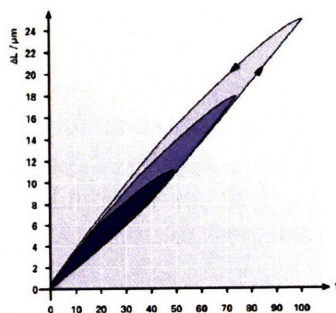


**Figure 10.** Hysteresis curve of a typical PZT.

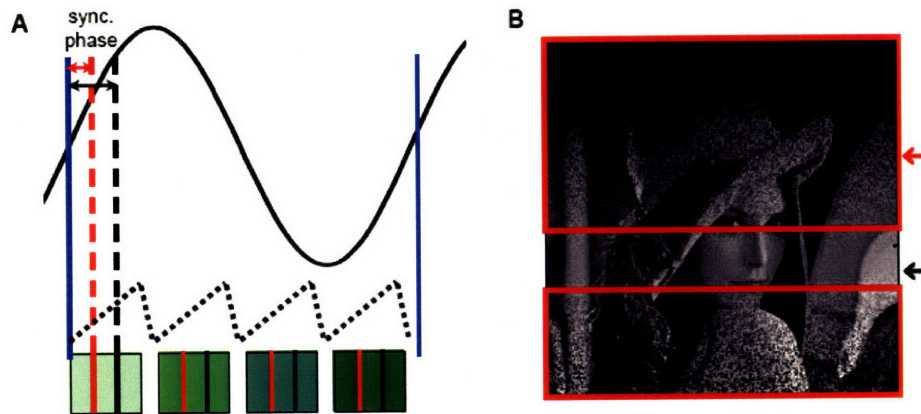


**Figure 11.** Simulation result showing that Dubois' algorithm fails when lines are collected to form an image before demodulation. (A) Modulation scheme. The black curve is the sinusoidal phase modulation and the dashed curve is the scanning waveform. The modulation depth is 4.9 rad. The colored blocks represent the four integration buckets required for demodulation. The red and black lines within the colored blocks represents two quadruplets with different synchronization phases. (B) Demodulation result. Due to the different synchronization phases, the two quadruplets result in a successfully demodulated line (black arrow) and an unsuccessfully demodulated line (red arrow).

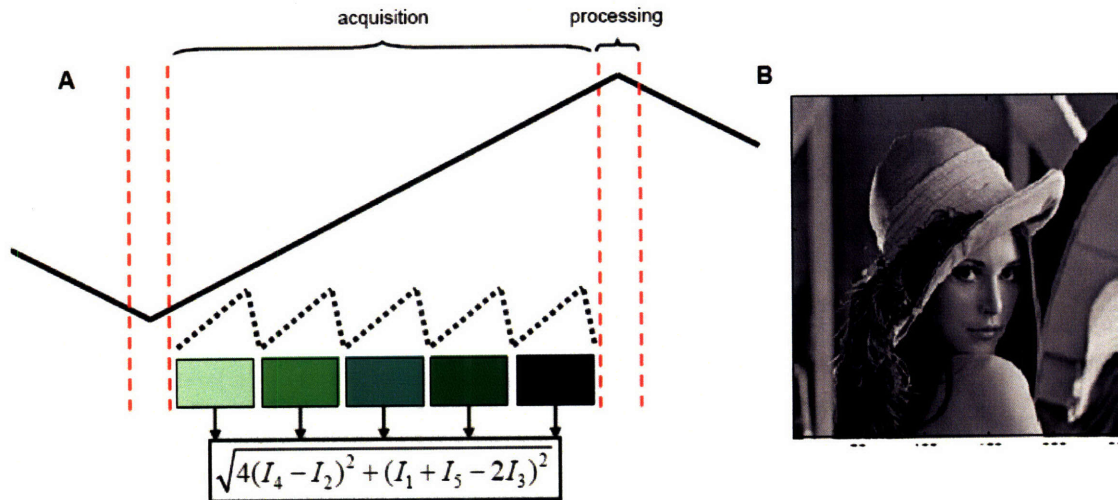


**Figure 11.** Simulation result of the proposed method. (A) Modulation scheme. The black curve is the triangular phase modulation and the dashed curve is the scanning waveform. The modulation depth is  $2.5\pi$ . The colored blocks represent the five integration buckets required for demodulation. Hariharan algorithm is chosen because of its strong robustness to errors. (B) Demodulation result.

| TD-OCM System Specifications                            | SS-OCM System Specifications                          | LS-OCM System Specifications                          |
|---|---|---|
| Coupled power from laser: ~ 44 mW                       | Coupled power from laser: ~ 12 mW                     | Coupled power from laser: ~ 90 mW                     |
| OCM sample power: ~10 mW                                | OCM sample power: ~1.5 mW                             | OCM sample power: ~25 mW                              |
| <u>Sensitivity: 98 dB</u>                               | <u>Sensitivity: 98 dB</u>                             | <u>Sensitivity: 92 dB</u>                             |
| <u>Center wavelength: ~ 1075 nm</u>                     | <u>Center wavelength: ~ 1290 nm</u>                   | <u>Center wavelength: ~ 820 nm</u>                    |
| Bandwidth (FWHM): ~ 140 nm                              | Bandwidth (FWHM): ~ 90 nm                             | Bandwidth (FWHM): ~ 80 nm                             |
| <u>Axial resolution: ~ 3.8 <math>\mu\text{m}</math></u> | <u>Axial resolution: ~ 8 <math>\mu\text{m}</math></u> | <u>Axial resolution: ~ 3 <math>\mu\text{m}</math></u> |
| Transverse resolution: ~ 1.7 $\mu\text{m}$              | Transverse resolution: ~ 1.6 $\mu\text{m}$            | Transverse resolution: ~ 2 $\mu\text{m}$              |
| FOV: ~ 390 x 390 $\mu\text{m}^2$                        | FOV: ~ 200 x 200 $\mu\text{m}^2$                      | FOV: ~ 250 x 250 $\mu\text{m}^2$                      |
| Frame rate: 2 Hz  | Frame rate: ~1 Hz                                     | Frame rate: ~ 2 Hz                                    |
| Image size: 500 x 750 pixels                            | Image size: 256 x 256 pixels                          | Image size: 250 x 250 pixels                          |

**Table 1.** Comparison of the three OCM systems.

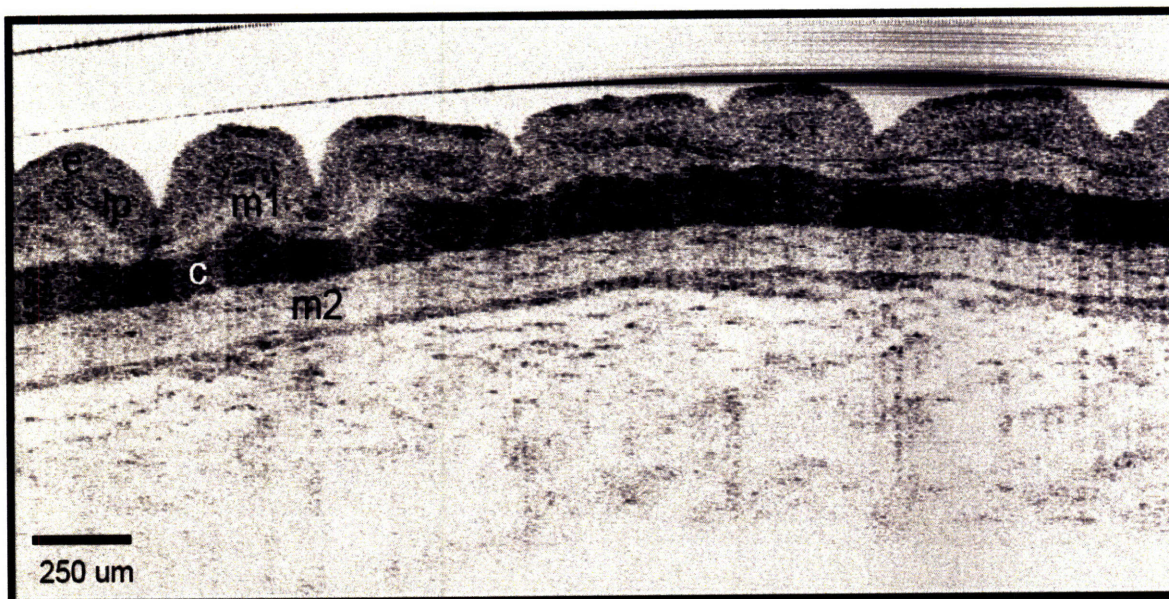


**Figure 13.** OCT image of a hamster cheek pouch *ex vivo*. Layered structure is clearly delineated. e, epithelium; lp, lamina propria; m1, superficial muscle layer; c, collagen-rich connective tissue; m2, deep muscle layer.

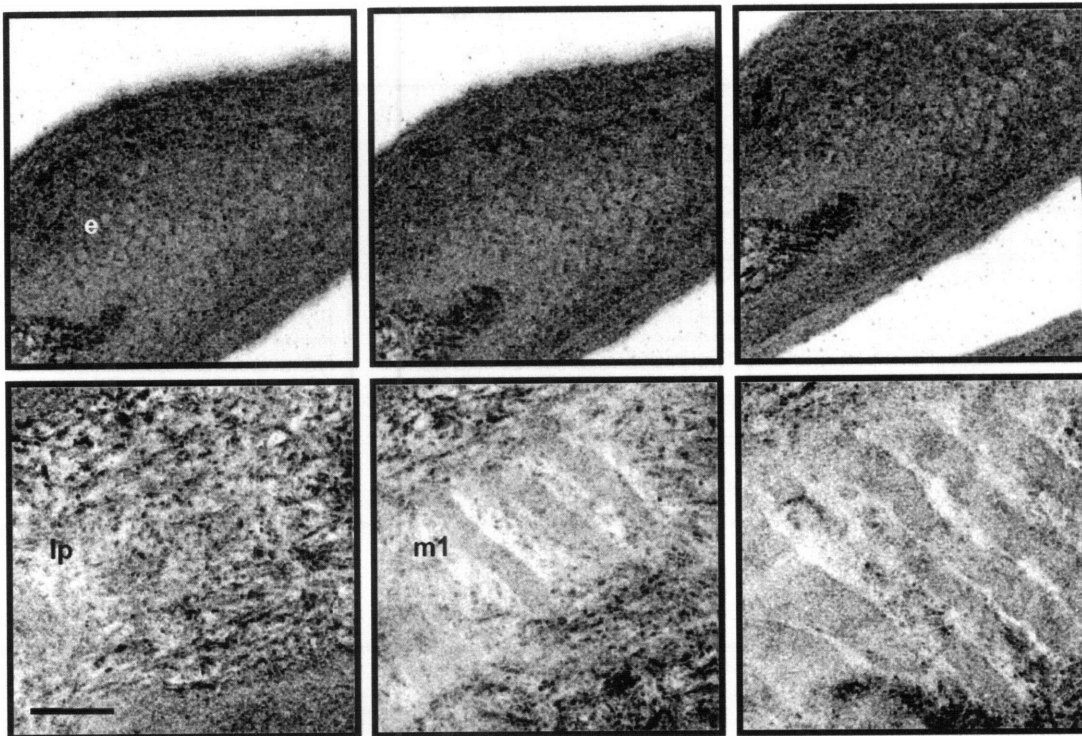


**Figure 14.** Time-domain OCM images of a hamster cheek pouch *ex vivo*. e, epithelium; lp, lamina propria; m1, superficial muscle layer. Scale bar: 100  $\mu\text{m}$ .

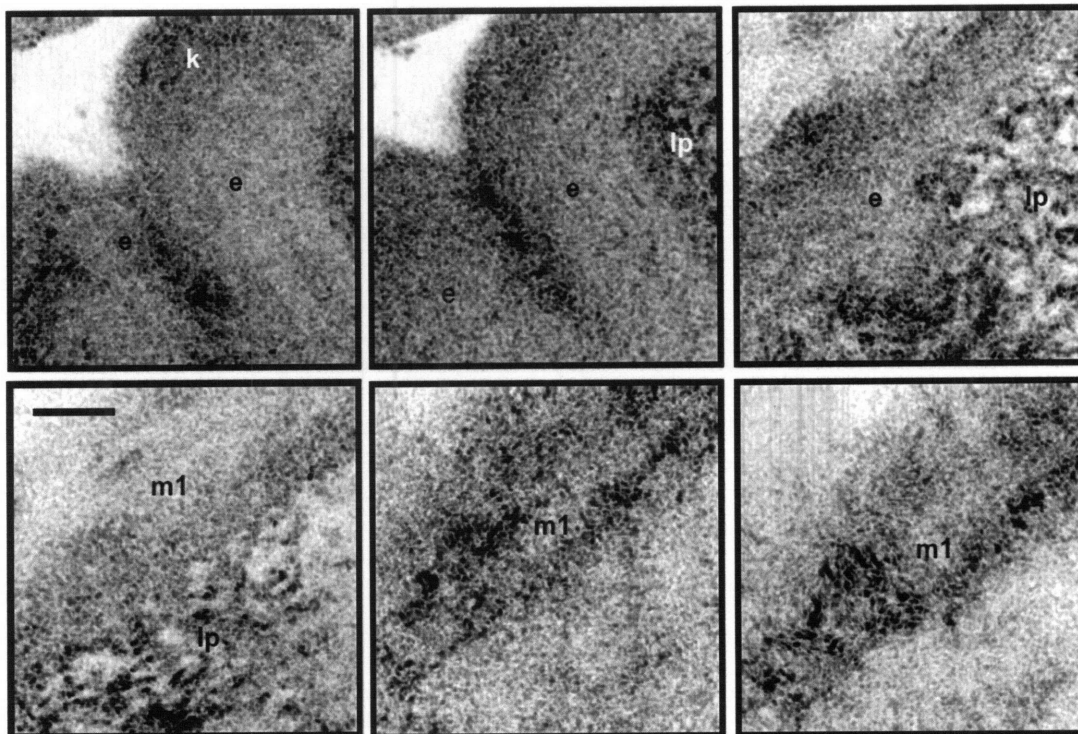


**Figure 15.** Swept source OCM images of a hamster cheek pouch *ex vivo*. e, epithelium; lp, lamina propria; m1, superficial muscle layer. Scale bar: 50  $\mu\text{m}$ .

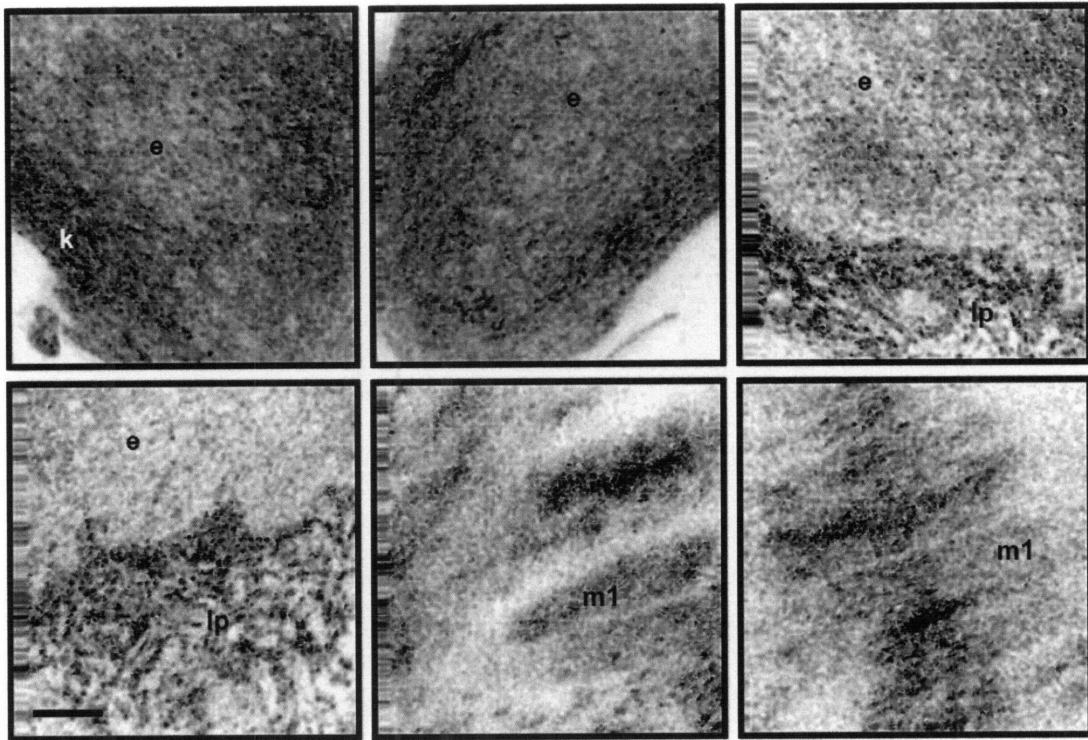


**Figure 16.** Line-scan OCM images of a hamster cheek pouch *ex vivo*. e, epithelium; lp, lamina propria; m1, superficial muscle layer. Scale bar: 50  $\mu\text{m}$ .

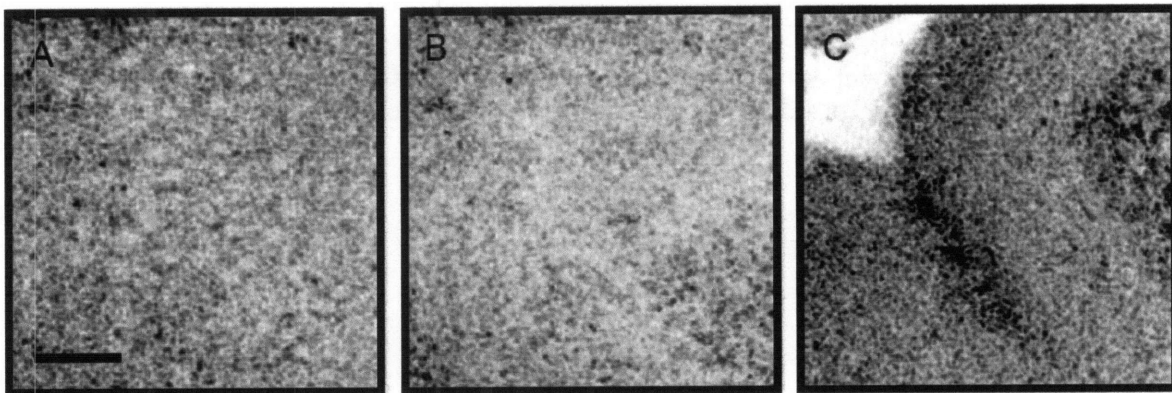


**Figure 17.** Comparison between swept source OCM and time domain OCM. (A) Epithelial cells can be clearly delineated in the time-domain OCM image. (B) To mimic the worse sectioning ability of swept source OCM, three time-domain OCM images at different depths are averaged and the result is shown. Loss of contrast is evident and there is no much difference from the image taken with swept source OCM, which is shown in (C). Scale bar: 50  $\mu\text{m}$ .

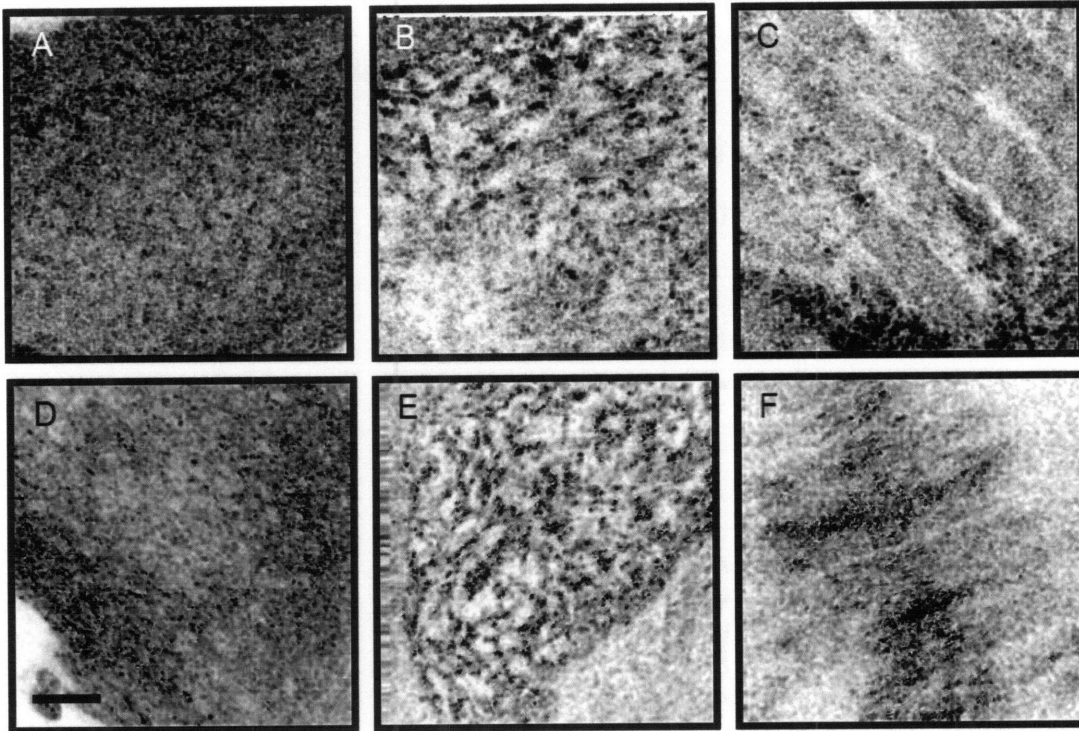


**Figure 18.** Comparison between line-scan OCM and time domain OCM. A-C: Time domain OCM images at epithelium, lamina propria, and superficial muscle layer. D-F: Line-scan OCM images at epithelium, lamina propria, and superficial muscle layer. Line-scan OCM shows images comparable to time domain OCM at shallow depth. Line-scan OCM has less speckles due to the time averaging effect. Image quality at deeper depth is considerably worse due to the higher scattering and lower system sensitivity. Scale bar: 50  $\mu\text{m}$ .

## References

- [1] C. J. R. Sheppard, M. Roy, and M. D. Sharma, "Image formation in low-coherence and confocal interference microscopes," *Applied Optics*, vol. 43, pp. 1493-1502, Mar 2004.
- [2] A. Dubois, L. Vabre, A.-C. Boccara, and E. Beaurepaire, "High-resolution full-field optical coherence tomography with a Linnik microscope," *Applied Optics*, vol. 41, pp. 805-812, Feb 2002.
- [3] A. Dubois, K. Grieve, G. Moneron, R. Lecaque, L. Vabre, and C. Boccara, "Ultrahigh-resolution full-field optical coherence tomography," *Appl Opt*, vol. 43, pp. 2874-2883, May 2004.
- [4] A. Dubois, G. Moneron, and C. Boccara, "Thermal-light full-field optical coherence tomography in the 1.2  $\mu$  m wavelength region," *Optics Communications*, vol. 266, pp. 738-743, Oct 2006.
- [5] M. Akiba, K. P. Chan, and N. Tanno, "Full-field optical coherence tomography by two-dimensional heterodyne detection with a pair of CCD cameras," *Optics Letters*, vol. 28, pp. 816-818, May 2003.
- [6] W. Y. Oh, B. E. Bouma, N. Iftimia, S. H. Yun, R. Yelin, and G. J. Tearney, "Ultrahigh-resolution full-field optical coherence microscopy using InGaAs camera," *Optics Express*, vol. 14, pp. 726-735, Jan 2006.
- [7] J. A. Izatt, M. R. Hee, G. M. Owen, E. A. Swanson, and J. G. Fujimoto, "Optical coherence microscopy in scattering media," *Optics Letters*, vol. 19, pp. 590-592, Apr 1994.
- [8] A. D. Aguirre, P. Hsiung, T. H. Ko, I. Hartl, and J. G. Fujimoto, "High-resolution optical coherence microscopy for high-speed, *in vivo* cellular imaging," *Optics Letters*, vol. 28, November 2003.
- [9] S. W. Huang, A. D. Aguirre, R. A. Huber, D. C. Adler, and J. G. Fujimoto, "Swept source optical coherence microscopy using a Fourier domain mode-locked laser," *Optics Express*, vol. 15, pp. 6210-6217, May 2007.
- [10] A. Jain, A. Kopa, Y. T. Pan, G. K. Fedder, and H. K. Xie, "A two-axis electrothermal micromirror for endoscopic optical coherence tomography," *Ieee Journal of Selected Topics in Quantum Electronics*, vol. 10, pp. 636-642, May-Jun 2004.
- [11] X. Liu, M. J. Cobb, Y. Chen, M. B. Kimmey, and X. Li, "Rapid-scanning forward-imaging miniature endoscope for real-time optical coherence tomography," *Opt Lett*, vol. 29, pp. 1763-1765, Aug 2004.
- [12] J. T. W. Yeow, V. X. D. Yang, A. Chahwan, M. L. Gordon, B. Qi, I. A. Vitkin, B. C. Wilson, and A. A. Goldenberg, "Micromachined 2-D scanner for 3-D optical coherence tomography," *Sensors and Actuators a-Physical*, vol. 117, pp. 331-340, Jan 2005.

- [13] W. Jung, D. T. McCormick, J. Zhang, L. Wang, N. C. Tien, and Z. P. Chen, "Three-dimensional endoscopic optical coherence tomography by use of a two-axis microelectromechanical scanning mirror," *Applied Physics Letters*, vol. 88, 163901, Apr 2006.
- [14] J. T. Liu, M. J. Mandella, H. Ra, L. K. Wong, O. Solgaard, G. S. Kino, W. Piyawattanametha, C. H. Contag, and T. D. Wang, "Miniature near-infrared dual-axes confocal microscope utilizing a two-dimensional microelectromechanical systems scanner," *Opt Lett*, vol. 32, pp. 256-258, Feb 2007.
- [15] A. Dubois, "Phase-map measurements by interferometry with sinusoidal phase modulation and four integrating buckets," *Journal of the Optical Society of America a-Optics Image Science and Vision*, vol. 18, pp. 1972-1979, Aug 2001.
- [16] K. Grieve, A. Dubois, M. Simonutti, M. Paques, J. Sahel, J. F. Le Gargasson, and C. Boccara, "In vivo anterior segment imaging in the rat eye with high speed white light full-field optical coherence tomography," *Optics Express*, vol. 13, pp. 6286-6295, Aug 2005.
- [17] P. Hariharan, B. F. Oreb, and T. Eiju, "Digital Phase-Shifting Interferometry - a Simple Error-Compensating Phase Calculation Algorithm," *Applied Optics*, vol. 26, pp. 2504-2506, Jul 1987.
- [18] M. A. Choma, M. V. Sarunic, C. H. Yang, and J. A. Izatt, "Sensitivity advantage of swept source and Fourier domain optical coherence tomography," *Optics Express*, vol. 11, pp. 2183-2189, Sep 2003.
- [19] J. F. de Boer, B. Cense, B. H. Park, M. C. Pierce, G. J. Tearney, and B. E. Bouma, "Improved signal-to-noise ratio in spectral-domain compared with time-domain optical coherence tomography," *Optics Letters*, vol. 28, pp. 2067-2069, Nov 2003.
- [20] R. Leitgeb, C. K. Hitzenberger, and A. F. Fercher, "Performance of Fourier domain vs. time domain optical coherence tomography," *Optics Express*, vol. 11, pp. 889-894, Apr 2003.
- [21] Y. Chen, S. W. Huang, A. D. Aguirre, and J. G. Fujimoto, "High-resolution line-scanning optical coherence microscopy," *Optics Letters*, vol. 32, pp. 1971-1973, Jul 2007.

## CHAPTER 4 – Summary

In summary, two novel designs for OCM systems, line-scanning optical coherence microscopy (LS-OCM) and swept source optical coherence microscopy (SS-OCM), are demonstrated. While time domain OCM so far provides the best imaging speed and quality, the two other techniques both have significant advantages.

SS-OCM is in essence swept source OCT with high numerical aperture optics. As such, it provides full three-dimensional volume acquisition within the confocal gate, which will allow multiple sections to be taken around the focal plane. The volumetric scan should make possible new approaches to compensate for shifts between the confocal and coherence gate and may enable volumetric as well as single slice cellular imaging. Since the technique shares the same principle as 3D-OCT, it will also facilitate combined state-of-art OCT and OCM imaging systems. Compared with previous implementations of time domain OCM, SS-OCM offers simplification in reference arm optical design at the expense of increased complexity in the detection electronics and need for increased computing power.

LS-OCM is a variation of full-field OCM, another emerging technology due to its simplicity and low-cost. Modification of the full-field OCM to accommodate line illumination and detection has several advantages. First, line illumination reduces pixel cross-talk and a weak confocal gate helps reject out-of-focus light. Together the sensitivity can be increased by more than an order of magnitude. Second, the correlation gate is widened so that gate coordination is not critical as it is for full-field OCM. Finally, line detection is less sensitive to sample motion compared with full-field detection because phase sensitive information is acquired more rapidly, before significant phase averaging effects can occur. Compared with confocal based OCM, LS-OCM requires only a single axis scanner in the sample arm and hence might facilitate the development of miniaturized probes for endoscopic applications.

Building on our recent advances in OCM system design, the future work will be focused on: 1) To develop a forward-scanning OCM probe to enable cellular level endoscopic imaging in the GI tract. 2) To develop an integrated OCM and OCT research microscope to enable comprehensive architectural and cellular level volumetric imaging in clinical pathology lab studies.

Endoscopic OCM will address some key limitations of current confocal endomicroscopy

techniques: 1. OCM probes can be designed with a larger field of view and increased imaging depth compared with confocal microscopy. 2. OCM uses combined confocal and optical coherence gating to image with enhanced penetration depth. 3. OCM images reflected light and does not require application of exogenous fluorescent dyes. In addition, OCM can leverage existing scanning probe technologies developed for confocal and multiphoton endoscopy. Therefore OCM offers a novel and powerful approach to endoscopic cellular imaging by combining advantages and technology from confocal microscopy and OCT.

Development of a flexible, small diameter endoscopic probe capable of cellular resolution imaging will be a major advance that promises to greatly improve current endoscopic techniques for early cancer detection as well as to expand the scope of applications for optical biopsy. Many research groups, including those in industry, are now actively developing endoscopic probes for OCT, confocal microscopy, and multiphoton microscopy. As a result, miniaturized optics, including microscope objectives, are now becoming available. Furthermore, a number of promising solutions to the challenging problem of two-axis scanning have been demonstrated. PZT actuation is very efficient in transforming electrical energy to mechanical energy, and therefore is especially attractive for high speed miniaturized scanning. We will investigate both the four-PZT actuator and the four-quadrant PZT device as previously described in the multiphoton microscopy literature [1, 2]. GRIN lenses have the advantage of small size and ready availability and hence will be used as the miniaturized near-infrared microscope objectives. We will also investigate focusing using suction techniques as previously described in confocal microscopy literature [3]. Application of mild suction between the objective and the tissue stabilizes the tissue and adjusts the focal depth. Suction can be accomplished as part of the device itself, or alternately, as part of an additional cap that is applied to the endoscope head similar to the caps currently used for endoscopic mucosal resection. The probes will have a waterproof sheath and will be designed to fit the working channel of standard endoscopes.

High imaging speeds allow rapid survey of large areas on tissue samples as well as increased throughput of tissue samples in an imaging study. In addition, high speed allows multi-frame averaging or acquisition of high pixel density images, which can be used to improve image quality or reduce speckle. Finally, high speed imaging allows visualization of dynamic processes such as blood flow. We will develop a bench-top, research microscope capable of imaging at video rate that can be used in pathology laboratory studies. The microscope will be

constructed using high-speed resonant scanners which allow raster line scan rates of 5-10 kHz and higher. The microscope will be equipped with variable magnifications through use of an objective lens turret similar to those used in standard bench microscopes. The use of high and low magnifications will allow combination of video-rate OCM and high-speed, swept source OCT in the same microscope. This imaging system will provide a comprehensive database of co-registered architectural and cellular level imaging of tissue samples. Such database for references has been proved to be extremely useful for histology, MRI, and CT communities.

## References

- [1] J. Sawinski and W. Denk, "Miniature random-access fiber scanner for in vivo multiphoton imaging," *Journal of Applied Physics*, vol. 102, pp. 5556-5564, Aug 2007.
- [2] M. T. Myaing, D. J. MacDonald, and X. D. Li, "Fiber-optic scanning two-photon fluorescence endoscope," *Optics Letters*, vol. 31, pp. 1076-1078, Apr 2006.
- [3] K. B. Sung, C. Liang, M. Descour, T. Collier, M. Follen, and R. Richards-Kortum, "Fiber-optic confocal reflectance microscope with miniature objective for in vivo imaging of human tissues," *IEEE Trans Biomed Eng*, vol. 49, pp. 1168-72, Oct 2002.

## APPENDIX

### 1. Sample preparations

The necessary animal and human studies protocols will be filed under accordance with MIT CAC and COUHES regulations.

#### –*Xenopus laevis* tadpole

1. 10-20 tadpoles will be housed in a 3 gallon standing water tank in our lab. They will be fed twice a week with tadpole powder purchased from Xenopus Express. The tank will be checked five hours after feeding and any uneaten food will be siphoned off to keep the water clear. Approximately 25% of the water will be changed once a week.
2. Five minutes prior to imaging, the tadpole will be anesthetized by immersion in 0.05% Tricane. We will achieve a depth of anesthesia in which the tadpole exhibits no gross movements for the purpose of imaging. All other body functions shall remain normal.
3. Imaging will be performed with the tadpole in water.
4. After imaging, the tadpole will be euthanized by immersion in 0.05% Benzocaine for 30 min followed by freezing at -20 °C. They will then be incinerated by the MIT DCM.

#### –Syrian golden hamster cheek pouch

1. Adult male Syrian hamsters (100 to 120 g) will be housed in the arranged MIT animal facility and fed laboratory chow and water ad libitum.
2. Ten minutes prior to imaging, the hamster will be euthanized following the AVMA guidelines for euthanasia through CO<sub>2</sub> gas inhalation in MIT animal facility. The hamster will then be brought back to our lab and trained personnel will excise the cheek pouch.
3. Imaging will be performed with the hamster cheek pouch immersed in phosphate-buffered saline.
4. After imaging, the carcass will be brought back to the arranged animal facility. They will then be incinerated by the MIT DCM.

**-Fixed rat kidney**

1. The fixed rat kidney samples are provided by Professor Peter M. Andrews from the Georgetown University and stored in the refrigerator.
2. Imaging will be performed with the specimen in water.
3. After imaging, the specimen will be put back in the refrigerator.

**-Excised human tissue**

1. The fresh excised human tissues will be provided by Dr. James Connolly from the Beth Israel Deaconess Medical Center and immersed in either phosphate-buffered saline or Dulbecco's Modified Eagle's Medium.
2. Imaging will be performed with the specimen immersed in phosphate-buffered saline.
3. After imaging, the specimen will be fixed in 1% formaldehyde and processed for histological comparison with the acquired images.